6.08 Amorphous and Nanocrystalline Silicon Solar Cells and Modules

S Guha, J Yang, and B Yan, United Solar Ovonic LLC, Troy, MI, USA

6.08.1	**Introduction**	309
6.08.2	**Deposition Methods**	311
6.08.2.1	Glow-Discharge Deposition Technique	311
6.08.2.1.1	Plasma chemistry and growth kinetics	311
6.08.2.1.2	Role of hydrogen dilution	312
6.08.2.1.3	Impurities	312
6.08.2.1.4	Deposition reactor	312
6.08.2.1.5	Frequency of applied power	312
6.08.2.2	Other Deposition Methods	313
6.08.3	**Material Properties**	313
6.08.3.1	Hydrogen Dilution Below the Edge (Amorphous Regime)	313
6.08.3.1.1	Film structure	313
6.08.3.1.2	Defect density	314
6.08.3.2	Hydrogen Dilution Above the Edge (Nanocrystalline Regime)	315
6.08.3.2.1	Structure	315
6.08.3.2.2	Impurities	315
6.08.3.2.3	Optical absorption	315
6.08.3.2.4	Defect density	316
6.08.4	**Single-Junction Cell**	316
6.08.4.1	Cell Structure	316
6.08.4.2	Cell Characteristic	317
6.08.4.3	Light-Induced Degradation	318
6.08.4.3.1	Amorphous silicon and silicon–germanium alloys	318
6.08.4.3.2	Nanocrystalline silicon	320
6.08.4.4	Cell Performance	321
6.08.4.5	High Deposition Rate	321
6.08.4.5.1	High-rate a-Si:H and a-SiGe:H solar cells	321
6.08.4.5.2	High-rate nc-Si:H solar cells	323
6.08.5	**Multijunction Cell**	324
6.08.5.1	Basic Structure	324
6.08.5.2	Key Requirements for Obtaining High Efficiency	325
6.08.5.2.1	BR for light trapping	325
6.08.5.2.2	Doped layers	328
6.08.5.2.3	Intrinsic layers	328
6.08.5.2.4	Current matching in multijunction solar cells	334
6.08.5.2.5	Tunnel junction	336
6.08.5.2.6	Top conducting oxide	337
6.08.5.3	High-Efficiency Solar Cell and Module	337
6.08.6	**Manufacturing Technology**	338
6.08.7	**Product Advantage and Market**	343
6.08.7.1	Product Advantage	343
6.08.7.2	Independent Verification of Performance	343
6.08.7.3	Market	344
References		347

Glossary

Amorphous silicon Silicon materials in a disordered state.
Antireflection coating A coating layer that reduces the reflectance from an object.
Back reflector A reflecting layer on the surface opposite to the surface through which light enters the solar cell.
Component cell A single-junction cell as a component in a multijunction solar cell.
Current matching A design of multijunction solar cells such that the photocurrent in each component cell is the same.
Dopant An impurity element added to semiconductor materials to change the conductivity of the materials.
Hydrogen dilution Using hydrogen gas to dilute silicon-containing and germanium-containing gases in glow discharge deposition.
Hydrogen dilution profiling Changes of hydrogen to silicon-containing gas with time during a glow discharge deposition.
Intrinsic layer A semiconductor layer without doping.
Light trapping Using textured back reflector to trap light in solar cells.
Meta-stable defect Defects that are created by light exposure, thermal quenching, or carrier injection. These defects can be removed by thermal annealing.
Microcrystalline silicon Silicon materials that contain small-sized crystallites in an amorphous matrix.
Multijunction solar cell A solar cell containing more than one p–n or p–i–n junction.
Nanocrystalline silicon The same as microcrystalline silicon, indicating crystallites with nanometer sizes.
Photovoltaic The effect of photo-induced electricity.
n-layer A semiconductor layer with n-type doping.
p-layer A semiconductor layer with p-type doping.
p–i–n junction A semiconductor device made with p-layer, intrinsic layer, and n-layer.
rf glow discharge A glow discharge sustained by a radio frequency of 13.56 MHz excitation.
Roll-to-roll deposition A continuous deposition method on flexible substrates using a roll-to-roll machine.
Single-junction solar cell A solar cell containing one p–n or p–i–n junction.
Solar array An array consisting of many solar modules.
Solar cell A device that converts sunlight into electricity.
Solar module A device with many interconnected solar cells.
Tunnel junction The n/p junctions in multijunction solar cells that connect two component cells.
vhf glow discharge A glow discharge sustained by a very high frequency.

Nomenclature

Eff or η	efficiency (%)
FF	fill factor
$\boldsymbol{J_{max}}$	current density at the maxima power ($mA\,cm^{-2}$)
$\boldsymbol{J_{sc}}$	short-circuit current density ($mA\,cm^{-2}$)
$\boldsymbol{N_s}$	defect density (cm^{-3})
$\boldsymbol{P_{max}}$	maximum power ($mW\,cm^{-2}$)
QE	quantum efficiency
$\boldsymbol{V_{max}}$	voltage at the maximum power (V)
$\boldsymbol{V_{oc}}$	open-circuit voltage (V)
λ	wavelength (nm)

6.08.1 Introduction

Hydrogenated amorphous silicon (a-Si:H) materials have received a great deal of attention for their potential to make inexpensive solar cells. The disorder inherent in the material allows it to absorb light efficiently. Only a thin film (less than 1 μm) is needed to absorb the sunlight rather than hundreds of micrometer (μm) that is needed for a conventional cell. The material cost is thus low. The film is grown using a plasma deposition process at a pressure of about 1 Torr and temperatures below 300 °C making

it viable for large-scale manufacturing. Since the first observation of doping in a-Si:H (Spear and LeComber, 1975) and subsequent demonstration of solar cells (Carlson and Wronski, 1976), there was high expectation that a-Si:H solar cells will dominate the photovoltaic (PV) market. Although significant advances were made in the laboratories, large-scale commercialization was slow to achieve. The conventional technology using single or polycrystalline solar cells still dominate the market, and the share of a-Si:H solar panels in the global market was only 8% in 2007. With the commercial successes achieved in the marketplace, several a-Si:H solar cell manufacturers have recently announced significant expansion of their capacity; there also have been reports of new entrants to the field building large-volume production facility. Analysts predict that while the PV market is going to grow annually by 25–30%, the growth for a-Si:H PV will be much faster – greater than 100%. Recent reports suggest production of a-Si:H PV will increase to 5000 MW in 2012 from the current level of about 200 MW in 2007 (PV News, August 2008).

Even though the low material cost and the ease of deposition make a-Si:H a very attractive candidate as a low-cost solar cell material, there are several challenges. a-Si:H is a very intriguing material. The absence of long-range order, which facilitates efficient photon absorption, causes tailing of the conduction and the valence band edges. The material also contains defects, such as dangling, strained, and weak bonds, that act as recombination centers for the electrons and the holes. The efficient operation of a solar cell depends on a two-step process – photon absorption for the generation of the carriers and subsequent carrier transport and collection. The presence of the recombination centers arising from the defects and the band tails hurts the transport and lowers the efficiency, even though the photon absorption is efficient. Incorporation of hydrogen reduces the defect density, and thus the material is in fact an alloy of amorphous silicon and hydrogen, and is referred to as hydrogenated amorphous silicon or amorphous silicon alloy. In spite of many advances made, the defect density is still much larger than that in crystalline silicon. The other challenge is the phenomenon of light-induced degradation (Staebler and Wronski, 1977). Exposure to light increases the defect density in the material and decreases the cell efficiency. While there has been tremendous progress in the understanding of the problem (Fritzsche, 2001), it still persists. The degradation, of course, is lower when the cell thickness is small since the photo-generated carriers do not have to travel a large distance. But that results in less absorption. Multijunction cells, where several cells can be stacked together, allow the use of individual cells with thin layers and achieve better stability. One can also use cells with intrinsic layers of different band gaps to capture photons of wider spectrum. A triple-junction cell structure where the middle and bottom cells use hydrogenated amorphous silicon–germanium alloys (a-SiGe:H) of different germanium content has already been commercialized (Yang *et al.*, 1997, 2003).

A major challenge facing the researchers has been to develop high-quality material with low defect density. The best-quality material is obtained by diluting the active gas with hydrogen (Guha *et al.*, 1981). With increase in hydrogen dilution, the material becomes more ordered, and beyond a certain critical dilution, it becomes nanocrystalline (also referred to as microcrystalline (Shah *et al.*, 2003)) with grains of about 10–30 nm size. The nanocrystalline material is a good absorber of light; the material is also stable against red light exposure. This is the spectrum that the bottom cell sees in a multijunction structure. Nanocrystalline silicon (nc-Si:H) is now getting increasing attention to replace a-SiGe:H in the bottom cells.

In this chapter, we discuss the advances made in the development of a-Si:H and nc-Si:H PV technology in terms of both improving the cell efficiency and devising low-cost manufacturing processes. Material properties that affect solar cell performance are briefly discussed; for detailed description of the physics of the materials, the readers are referred to other treatises (Street, 1991; Fritzsche, 1988). In Section 6.08.2, we describe the deposition methods that are used to obtain a-Si:H and nc-Si:H materials and solar cells. The material properties are discussed in Section 6.08.3. In Section 6.08.4 we discuss the simplest solar cell structure and its theory of operation. The phenomenon of light-induced degradation in a-Si:H and nc-Si:H and its effect on cell performance are also discussed. In Section 6.08.5, we outline the multijunction approach and the advantages of using a-SiGe:H with different band gaps or nc-Si:H to capture photons of a wider spectrum. Manufacturing methods are outlined in Section 6.08.6, and products and performance are discussed in Section 6.08.7.

6.08.2 Deposition Methods

6.08.2.1 Glow-Discharge Deposition Technique

Although a variety of techniques have been used (Luft and Tsuo, 1993) to deposit a-Si:H materials and solar cells, the most common method is still the glow-discharge deposition (also referred to as plasma-enhanced or plasma-assisted chemical vapor deposition). A silicon-containing gas, usually silane, is introduced into a vacuum chamber. The glow discharge is initiated by applying a direct current (DC) or an alternating current (13.56–200 MHz frequency) power input to a pair of electrodes. A typical reactor (**Figure 1**) consists of a gas inlet arrangement, a deposition chamber that holds the pair of electrodes and a substrate heating assembly, a pumping system, and a source of power for the discharge.

6.08.2.1.1 Plasma chemistry and growth kinetics

The growth of the film on the substrate takes place through four different stages (Matsuda *et al.*, 2003). In the first stage, electrons collide with silane to dissociate the silane molecules into a mixture of reactive species of ions and free radicals. The second stage is the drifting or diffusion of these species to the surface of the substrate during which time there is a multiplicity of secondary reactions. In the third stage, the different species are adsorbed onto or react with the growing surface, and finally, these species or their reaction products are incorporated into the growing film or are reemitted from the surface into the gas phase.

Detailed analysis of the deposition process has been provided by several researchers (Doyle *et al.*, 1992a, 1992b; Gallagher *et al.*, 2003; Matsuda, 1999; Matsuda and Tanaka, 1982). Electron–molecule collisions dissociate the molecules into ions and neutral radicals. These radicals undergo various secondary reactions during their transport to the substrate creating many different species of Si_xH_y. Incorporation of hydrogen in the film is determined by both the precursors in the plasma and growth kinetics at the growing surface. The quality of the film improves with incorporation of hydrogen that saturates the dangling bonds. Excess hydrogen and also presence of di- and polyhydrides in the film can create excessive void density in the material degrading its PV properties. The deposition parameters thus critically control the suitability of the material for PV application. In a typical system using radio frequency (rf) glow discharge, the following deposition parameters are used: pressure 0.5–2 Torr; electrode separation 3–6 cm; temperature 150–300 °C; and power density 10–100 mW cm^{-2}. The gas-flow rate depends on the volume of the chamber and area of the electrodes. Typically, one maintains adequate gas flow to avoid causing depletion of the active gas.

Deviating from the above standard conditions in general creates poorer-quality material. Higher power and pressure can lead to powder formation in the chamber. Lower temperature causes larger hydrogen content in the film, leading to high microvoid density. Higher temperature, however, causes hydrogen to effuse, creating dangling bonds. Some of the special conditions when one can deviate from the standard and still get good-quality material are discussed later.

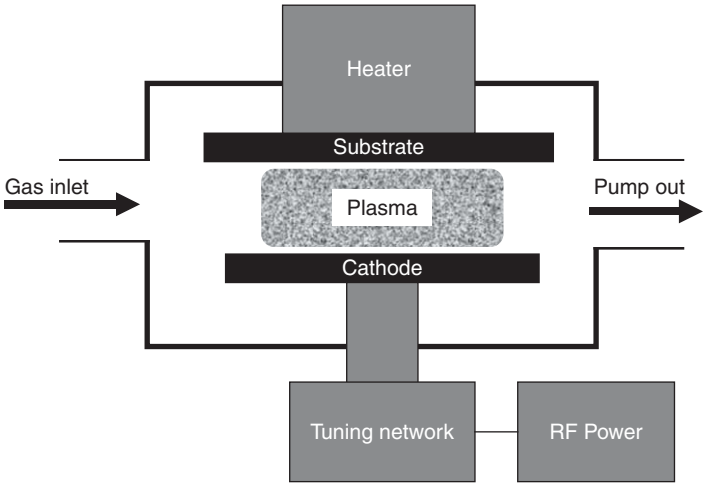

Figure 1 Schematic diagram of a glow-discharge deposition reactor.

6.08.2.1.2 Role of hydrogen dilution

While all the above parameters determine the film quality, hydrogen dilution has played a major role in improving material and cell performance. It was first shown by Guha *et al.* (1981) that films grown with a gas mixture of silane diluted with hydrogen have improved quality. Hydrogen dilution is now used extensively for obtaining high-quality a-Si:H, a-SiGe:H, and a-SiC:H materials with many different active gases. What is the role of excess hydrogen in the plasma? It provides improved surface coverage resulting in the impinging molecules diffusing further to find more energetically favorable sites (Robertson, 2000a, 2000b). Hydrogen dilution should, therefore, result in a more ordered structure; in fact, with increasing hydrogen dilution, one should expect growth of microcrystallites. This has been known for a long time. Hydrogen is also an etchant. During the deposition process, both ordered and disordered regions may be deposited simultaneously, and hydrogen etches away the disordered regions more effectively, leaving behind the ordered structure (Matsuda *et al.*, 1983). An alternative explanation for obtaining a more ordered structure with hydrogen dilution is the phenomenon of chemical annealing (Tsai *et al.*, 1989). This model postulates the structural relaxation of the amorphous phase and transition to crystalline phase by permeation of hydrogen atoms to a subsurface region. It has been recently (Fujiwara *et al.*, 2000; Shibata *et al.*, 1987) demonstrated that atomic hydrogen can be inserted into strained Si–Si bonds in the subsurface region through the formation of a SiH_n complex. Subsequent structural relaxation of these bonds results in the growth of a more ordered phase. Molecular dynamics simulations also support this model (Sriraman *et al.*, 2002).

While all the above models are consistent with the observation of improved order with increasing hydrogen dilution, an alternative explanation has been put forward (Roca i Cabarrocas, 2000; Longeaud *et al.*, 1998; Meaudre *et al.*, 1999) on the basis of formation of silicon powder (nanoclusters) in the plasma and their subsequent incorporation in the film. The deposition conditions and the hydrogen dilution are similar to those that have been used for obtaining high-quality materials described earlier.

As described earlier, as the hydrogen dilution increases, the material becomes more ordered and, beyond a certain dilution, it becomes microcrystalline or nanocrystalline. The hydrogen-to-active gas dilution ratio at the transition is determined by many factors and is typically in the range of 10–20. It has been observed that the amorphous material just below the edge to the transition is of the highest quality. Similarly, the material grown just above the edge also results in the highest-quality nc-Si:H (Roschek *et al.*, 2000). Growth of high-quality nc-Si:H has also been achieved by using high pressure (up to 10 Torr) and in the silane-depletion regime (Kondo, 2003). The basic idea is to reduce ion bombardment by using high pressure and increase atomic hydrogen density by depleting silane.

6.08.2.1.3 Impurities

There are two types of impurities that affect material and cell performance. Conventional dopants such as P and B will shift the Fermi level and affect carrier transport. These impurities must be kept lower than $10^{16}\,cm^{-3}$. The other category includes typical impurities in a vacuum system such as oxygen, nitrogen, and carbon. These can give rise to states in the gap that will act as recombination centers. It has been shown (Kinoshita *et al.*, 1996; Tsai *et al.*, 1984) that the quality of the material is unaffected if content of these impurities can be kept below $10^{19}\,cm^{-3}$. This can be routinely achieved when conventional precautions as applicable to vacuum systems are taken while designing the deposition reactor.

6.08.2.1.4 Deposition reactor

The simple reactor shown in **Figure 1** suffers from two limitations. First, the system has to be vented to atmosphere after every deposition run, and the atmospheric water vapor and oxygen that cling to the wall of the chamber take a very long time to be eliminated. Second, when dopant gases are used to make the doped layers in the solar cells, a trace amount of those impurities gets incorporated in the intrinsic layer as well. This is undesirable. A multichamber load-locked system (**Figure 2**) is, therefore, usually used for deposition of high-quality solar cells. By using dedicated chambers separated by gate valves for growing the doped and undoped layers, cross contamination can be reduced to acceptable levels. After the deposition is completed, only the load chamber needs to be vented to atmosphere, and the growth chambers are not exposed to atmosphere in between deposition runs.

6.08.2.1.5 Frequency of applied power

Most of the reported glow-discharge systems use an rf frequency of 13.56 MHz. Very high frequency (vhf) has recently been used successfully to grow both amorphous and nanocrystalline silicon materials. It was first shown by the Neuchatel group (Curtins

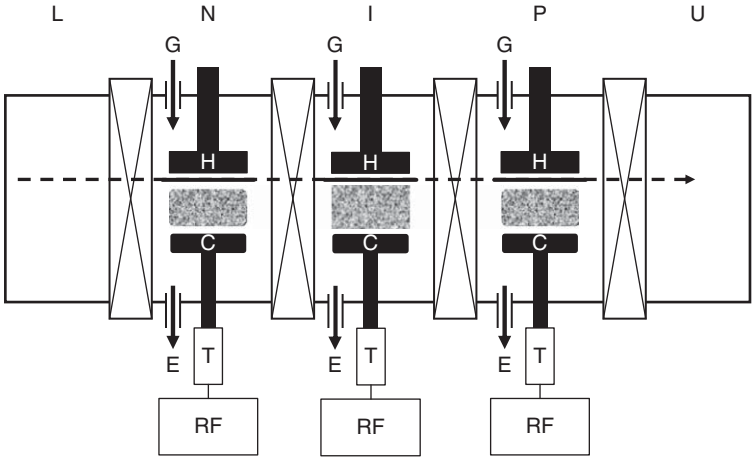

Figure 2 A schematic diagram of a load-lock multichamber system with a loading chamber (L), N chamber, I chamber, P chamber, and unload chamber (U). G denotes the gas inlet, E the exhaust system, H the heater, C the cathode, T tuning network, and RF the RF power supply. The dashed arrow shows the substrates moving direction.

et al., 1987a, 1987b; Shah *et al.*, 1992) that as the plasma excitation frequency is increased the deposition rate could be enhanced. The technique has now been used successfully to obtain high-efficiency solar cells based on both amorphous and nanocrystalline silicon materials. Yan *et al.* (1999) measured the ionic energy distribution for rf and vhf plasmas and found that the ionic energy distribution shifts to lower energy for vhf plasma. By contrast, the ionic flux is much higher. This explains the high deposition rate obtained using vhf, and it is believed that intense low-energy bombardment results in a more compact structure with high quality. The vhf method has also been successfully used to obtain high-quality nc-Si:H alloy cells (Shah *et al.*, 2003).

Microwave frequencies have also been successfully used to deposit a-Si:H alloys. Both electron cyclotron resonance chemical vapor deposition (ECR-CVD) (Ichikawa *et al.*, 1987; Sakamoto, 1977; Dalal *et al.*, 1997) and microwave plasma CVD (Guha *et al.*, 1994) have been used to make good-quality devices. The advantage of ECR-CVD is to control the ion energy. Although very high deposition rates have been demonstrated in the laboratories, the issue of cell degradation has prevented these techniques from being used in commercial production.

6.08.2.2 Other Deposition Methods

Many other techniques have been used to deposit a-Si:H and a-SiGe:H materials. Hot-wire CVD (HWCVD) deposition (also known as catalytic CVD) has been investigated in several laboratories (Mahan, 2003; Mahan *et al.*, 1991; Matsumura, 1987; Matsumura and Tachibana, 1985). In this method, a tungsten filament is heated to 1400–2000 °C in the reactor to cause thermal decomposition of the active gas. It is generally believed that unlike in the PECVD plasma, HWCVD plasma contains minimal number of higher silane species and is free from high-energy ions; both these features can give rise to superior film quality. HWCVD has produced films with very low H-content and good stability (Mahan *et al.*, 1991; Mahan, 2003). Nanocrystalline silicon materials at high deposition rates have also been obtained. So far, the process is still far away from commercial exploitation.

Sputtering in a partial pressure of hydrogen, electron beam deposition, inductively coupled plasma deposition, and many other techniques are also being pursued in different laboratories (Goto *et al.*, 1997; Miller *et al.*, 1978; Moustakas *et al.*, 1985; Nuruddin *et al.*, 1992; Shimizu *et al.*, 1986).

6.08.3 Material Properties

6.08.3.1 Hydrogen Dilution Below the Edge (Amorphous Regime)

6.08.3.1.1 Film structure

The first systematic investigation of the effect of hydrogen dilution on the structure of a-Si:H alloys was carried out by Tsu *et al.* (1997) using high-resolution transmission electron microscopy (TEM) and Raman spectroscopy. The TEM results showed that embedded in the amorphous matrix are chain-like objects (CLOs)

having ~3 nm width, ~30 nm length, and a high degree of order along their length. The density of the CLOs increases with increasing hydrogen dilution. At very high hydrogen dilution, TEM results show the formation of nanocrystallite inclusions; it is interesting to point out that small nanocrystallites are observed even in films that are deposited below the threshold under conditions that are used for making the intrinsic alloys for the highest-quality cells.

Raman measurements show a continuous shift of the TO peak 475 cm^{-1} to higher wave numbers with increasing hydrogen dilution. The results are interpreted by assigning a TO band existing at 490 cm^{-1} that exists in all the samples but increases in magnitude with increasing hydrogen dilution. This band is inferred to be the signature of the intermediate-ordered CLOs. The Raman peak associated with nanocrystallites at ~515 cm^{-1} is observed in over-the-edge samples.

X-ray diffraction (XRD) measurements have also been used (Williamson, 2003) to investigate the structure of these films. A narrowing of the width of the first X-ray scattering peak is observed with increasing hydrogen dilution indicating improved intermediate-range order. At dilutions above the threshold, microcrystallites appear with significant narrowing of the width of the peak (3° as opposed to more than 5°).

A thickness dependence of the structure of the films was also demonstrated by these studies (Guha *et al.*, 1999b). Films of different thicknesses grown under the same deposition conditions show improvement in intermediate-range order as the thickness increases.

Similar dependence of degree of order on hydrogen dilution was reported by Koh *et al.* (1998, 1999) using real-time spectroscopic ellipsometry. A thickness versus hydrogen dilution phase diagram was proposed, and the region of the phase diagram near the phase boundary but below the onset was termed the protocrystalline regime. Real-time spectroscopic ellipsometry is an important tool to study the evolution of film growth, and the work has elucidated valuable information about the structure of films and its correlation with device performance (Collins *et al.*, 2003).

6.08.3.1.2 Defect density

Sub-band-gap absorption (Xu *et al.*, 1996) of a-Si:H and a-SiGe:H materials was measured by constant photocurrent method (CPM) and showed very little effect of hydrogen dilution on defect density (**Table 1**). Both the initial and degraded defect densities were similar within experimental uncertainty. The cell performance, by contrast, was much better with high dilution.

It has been argued (Xu *et al.*, 1993) that since CPM measurements are carried out on films parallel to the surface whereas the cell performance is measured in the perpendicular direction, a better correlation may be obtained if the defect density could be measured in an actual cell structure. This is especially important if the material is heterogeneous as is the case with hydrogen-diluted alloys. Drive-level capacitance profiling (DLCP) is an interesting tool (Michelson *et al.*, 1985) since it can measure defect density in the actual cell configuration. Measurements using DLCP (Guha *et al.*, 1999) show reduction in defect density as the hydrogen dilution is increased. What is most interesting is the fact that the defect density shows a spatial nonuniformity in the on-the-edge material, with the density decreasing in the growth direction. This demonstrates the improvement of order with thickness, confirming the earlier SAXS measurements.

Table 1 Defect density in films and efficiency of cells at different hydrogen dilution

Sample no.	*Description*	*N_s, initial (CPM) (cm^{-3})*	*N_s, degraded (CPM) (cm^{-3})*	*P_{max} (initial) ($mW\,cm^{-2}$)*	*P_{max} (degraded) ($mW\,cm^{-2}$)*
1	a-Si:H, 300 °C, low H_2 dilution	2.9 e15	2.9 e16	7.5	5.8
2	a-Si:H, 300 °C, high H_2 dilution	4.4 e15	3.0 e16	7.6	6.4
3	a-Si:H, 175 °C, low H_2 dilution	7.9 e15	3.0 e16	7.0	4.0
4	a-Si:H, 175 °C, high H_2 dilution	5.0 e15	2.5 e16	7.5	6.1

6.08.3.2 Hydrogen Dilution Above the Edge (Nanocrystalline Regime)

As the hydrogen dilution increases, the transition to the nanocrystalline phase takes place. The material is characterized by formation of nanocrystallites; the volume fraction and the size of the nanocrystallites grow with increasing hydrogen dilution. **Figure 3** shows a schematic of nanostructure evolution as hydrogen dilution increases.

The tiny crystallites grow with increasing hydrogen dilution, forming cone-shaped structures as the hydrogen dilution further increases. For very dilute mixtures, columnar growth starts taking place and cracks develop in the film with adverse effects on material quality. The best material is thus grown just above the edge of hydrogen dilution for amorphous to nanocrystalline transition (Roschek *et al.*, 2000).

6.08.3.2.1 Structure

The film shows a profound inhomogeneity in the growth direction as can be seen by TEM and atomic force microscopy (AFM) micrographs. One starts with an amorphous zone followed by a layer consisting of a mixture of amorphous and nanocrystallites. Finally, cone-shaped structures appear (Jiang *et al.*, 2008) containing large number of nanometer-sized grains. It has been suggested (Teplin *et al.*, 2008) that once a nano-sized grain is formed, the grain could have a higher sticking coefficient or a lower surface mobility than the surrounding amorphous region, leading to a rapid growth in this area. A cone kinetics model has been developed (Teplin *et al.*, 2008), which explains the observed cone angle of 40° if the nano-grains grow about 30% faster than the surrounding a-Si:H area.

The increase in grain size with increasing thickness has been confirmed by Yan *et al.* (2004c, 2004d) from AFM, X-ray diffraction, and Raman studies. **Figure 4** shows the AFM picture of two films of different thicknesses. Note that the surface roughness of the 2-μm-thick film is much larger indicating larger crystallites for the thicker film. XRD signal also increases with increasing film thickness by an order of magnitude as the film thickness increases from 0.3 to 2 μm, and Raman studies indicate the volume fraction to increase from 60 to 80% for the two films. Raman results using different wavelengths also confirm the volume fraction increase in the growth direction of the film.

6.08.3.2.2 Impurities

Unlike in the case of a-Si:H alloy, oxygen is a donor in nc-Si:H alloy. This is believed to be due to oxygen incorporation at the grain boundaries, and nc-Si:H alloy is usually n-type (Wang and Lucovsky, 1990). Low amount of oxygen in the film is necessary to improve quality. Use of *in situ* purifiers (Meier *et al.*, 1996) and design of systems with high vacuum compatibility are some of the approaches that have been adopted to reduce oxygen content in the film. Deposition at low substrate temperature (<180 °C) has also been reported to reduce the donor concentration in the film caused by oxygen impurity. Since the oxygen content is similar, this is attributed to the different configuration of the oxygen-related defect for these films (Nasuno *et al.*, 2000).

6.08.3.2.3 Optical absorption

Typical as-measured optical absorption spectrum for nc-Si:H films is shown in **Figure 5** (Shah *et al.*, 2003)

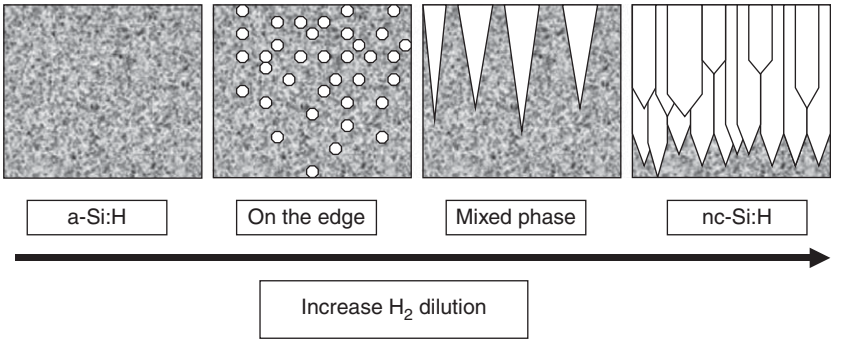

Figure 3 A schematic drawing of material structure changes as increasing hydrogen dilution. At low (or no) hydrogen dilution, the material shows homogeneous a-Si:H structure; at a relative high hydrogen dilution, isolated nano-grains are formed inside the amorphous matrix, increasing hydrogen dilution further, cone-shaped nanocrystalline clusters are formed, and at very high hydrogen dilution, columnar-structured nanocrystalline clusters are formed.

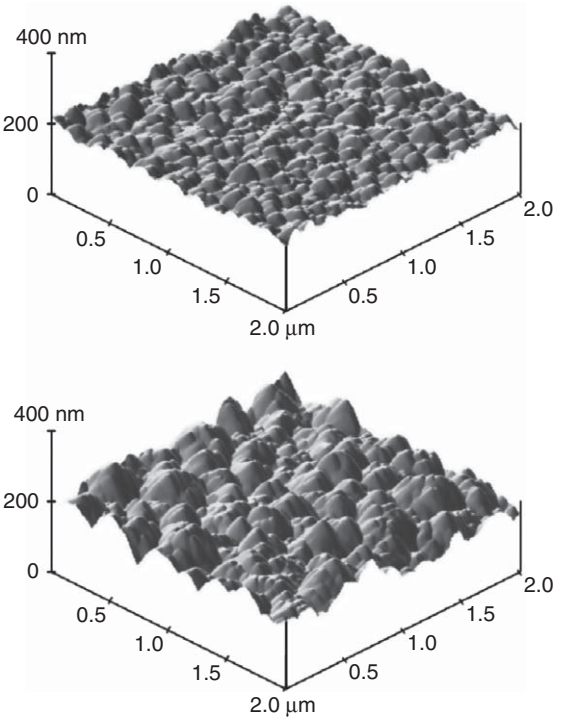

Figure 4 AFM images of two nc-Si:H solar cells with different thicknesses. From Yan B, Yue G, Yang J, *et al*. (2004d) Microstructure evolution with thickness and hydrogen dilution profile in microcrystalline silicon solar cells. *Materials Research Society Symposium Proceedings* 808: 575–580.

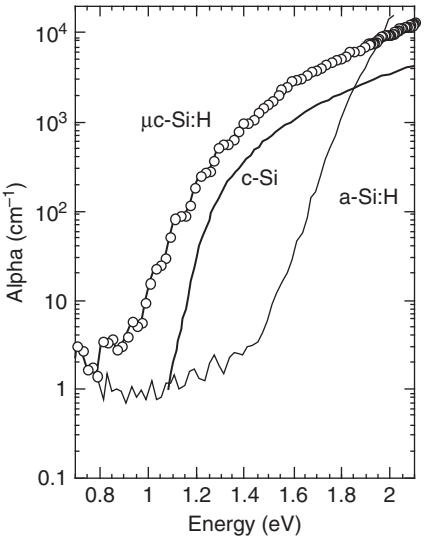

Figure 5 Absorption spectra of a-Si:H, c-Si, and nc-Si:H. From Shah AV, Meier J, Vallat-Sauvain E, *et al*. (2003) Material and solar cell research in microcrystalline silicon. *Solar Energy Materials and Solar Cells* 78: 469–491.

and compared with that for a-Si:H and crystalline silicon. The absorption curve for nc-Si:H closely follows the shape of crystalline silicon in the energy range higher than 1.4 eV. The absorption coefficient is higher, believed to be caused by light scattering at the textured surface. The increase in absorption above 1.8 eV could also be caused by the presence of the amorphous phase. The sub-band-gap absorption is high, again caused by scattering from the rough surface and interfaces. The net effect is an enhanced red response of the quantum efficiency (QE) in nc-Si:H alloy cells, as discussed later.

6.08.3.2.4 Defect density

Sub-band-gap absorption measurement in nc-Si:H, where scattering due to texture is removed, indicates a defect density (Poruba *et al*., 2000) much lower than that in a-Si:H. The heterogeneous nature of the material makes it difficult to make an unambiguous determination of defect density from electron spin resonance (ESR) measurements. Hugger *et al*. (2008) have carried out detailed measurements on defect density on nc-SiH with different crystalline volume fraction using deep level capacitance profiling, transient photocapacitance, and transient photocurrent spectroscopy. In general, defect density is lower than in a-Si:H; interpretation of the distribution is rather complex.

6.08.4 Single-Junction Cell

6.08.4.1 Cell Structure

The a-Si:H and nc-Si:H alloy solar cells can be fabricated using a variety of structures such as metal–semiconductor (Schottky diode), metal–insulator–semiconductor diode, p–n junction and p–i–n junction. As in the case of single crystals, the first two structures do not produce high-efficiency devices since the voltage generated is determined by the interface properties and is usually low. Since the incorporation of the dopant atoms in the intrinsic material increases the defect density and hinders carrier transport, it is desirable that the photon absorption and carrier transport take place in the intrinsic (i) layer only, and the highest efficiencies are obtained only with the p–i–n structures. The two commonly used structures are shown in **Figure 6**. In one configuration (case a, also known as substrate-type structure), the a-Si:H alloy layers are deposited on a metal substrate (e.g., stainless steel) or on an insulating substrate coated with a

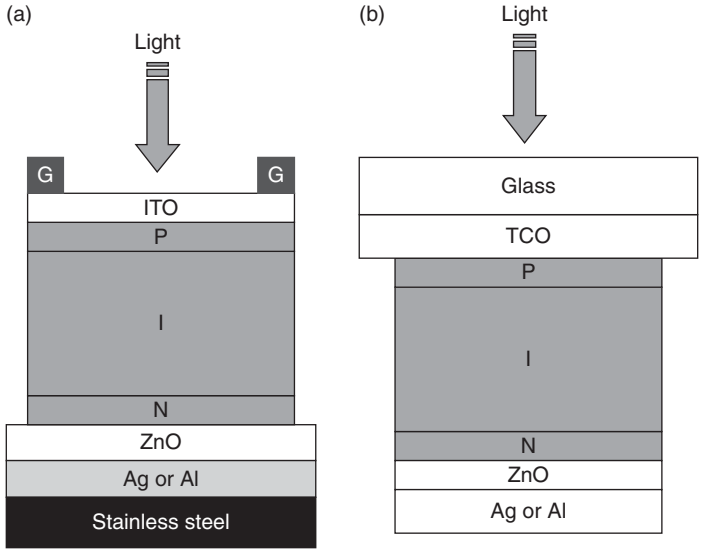

Figure 6 Schematic diagram of (a) substrate-type and (b) superstrate-type a-Si:H p–i–n solar cell structures.

metal. The metal forms one electrode of the cell and an ohmic contact to the heavily doped n-type layer. The top contact is the transparent conducting oxide layer through which the light enters. This oxide layer, which is typically indium tin oxide (ITO), forms an ohmic contact to the heavily doped p-type layer and also serves as an antireflection coating. In the other configuration (case b, also known as the superstrate-type structure), the transparent conducting oxide layer is deposited on glass through which the light enters. The a-Si:H alloy layers are deposited consecutively on top of this oxide, which is typically zinc oxide or tin oxide. A metal film is finally deposited to complete the cell structure.

6.08.4.2 Cell Characteristic

Light entering into the i-layer is absorbed to create the electron–hole pairs. These carriers move toward the electrodes by a process of drift and diffusion. A typical current–voltage characteristic of a solar cell under illumination is shown in Figure 7. Three parameters define the performance: the open-circuit voltage (V_{oc}), the short-circuit current (I_{sc}), and the fill factor (FF). The FF is the ratio of the product of the voltage and the current obtained at the maximum power point to that of V_{oc} and I_{sc}, where V_{oc} and I_{sc} are the values of the voltage and the current obtained under illumination when $I = 0$ and $V = 0$, respectively.

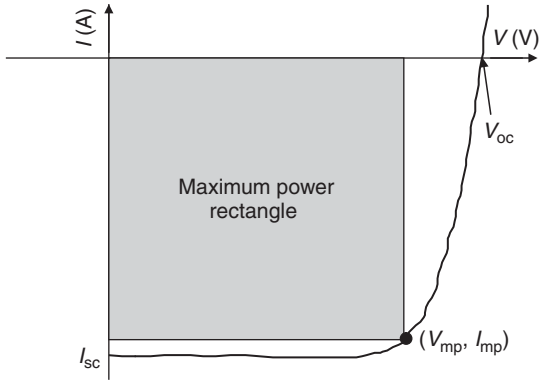

Figure 7 Current–voltage characteristics of a solar cell.

The efficiency of the cell that is given by the ratio of the power output to the power input is given by

$$\eta = \frac{V_{oc} \times \mathcal{J}_{sc} \times FF}{P_{input}}$$

where $\mathcal{J}_{sc}$, the short-circuit current density, is I_{sc} per unit area. The open-circuit voltage is determined by the built-in potential in the device, which, in turn, is dictated by the band gap. The larger the band gap, the higher will be the value of V_{oc}. However, as discussed earlier, the gap states present in the material act as recombination centers, and V_{oc} is governed by the separation of the electron and hole quasi-Fermi levels under illumination. Since this separation is determined by the gap-state density, V_{oc} is determined by both the band gap and the gap-state density.

The short-circuit current density is determined by the number of the absorbed photons, which, in turn, depends on the band gap of the material and the thickness of the i-layer. As the band gap is lowered, J_{sc} increases. The thickness of the i-layer cannot be increased indefinitely for increased photon absorption to obtain higher J_{sc}. The gap states limit the effective length that the carriers can move before recombining, and increasing the thickness beyond certain collection length does not result in any further improvement of J_{sc}. The FF determines how efficiently the carriers are collected. This is also determined by the i-layer thickness and the gap-state density. In order to design a cell to obtain the highest efficiency, all the above factors need to be considered carefully.

To have a proper understanding of the various material parameters on the cell performance, numerical models have been developed (Arch *et al.*, 1991; Hack and Shur, 1985; Pawlikiewicz and Guha, 1990; Wang *et al.*, 1996), which solve the Poisson and current-continuity equations across the p–i–n structure. Knowledge about the gap-state distribution and other material parameters is necessary for the simulation studies. As mentioned earlier, the absence of long-range order causes tailing of the band edges. The presence of dangling, weak, and strained bonds, impurities, and defect–impurity complexes can also result in gap states. The net effect is a continuous distribution of states in the mobility gap. A typical gap-state distribution is shown in **Figure 8**. The valence band tail has a characteristic energy of about 50 meV and is wider than the conduction-band tail, which has a characteristic energy of about 25 meV. The mid-gap states, defined as D_o, are caused by the neutral dangling bonds. Depending on the position of the Fermi level, these states can get charged occupying new positions D^- and D^+.

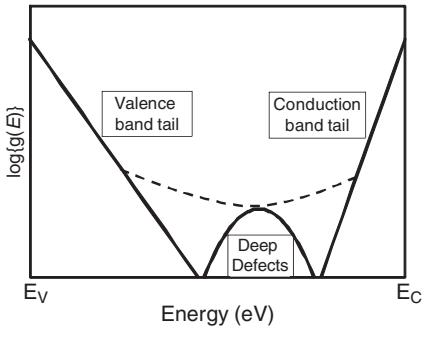

Figure 8 Gap-state distribution of a-Si:H materials.

In addition, impurities and other defects can result in a continuous distribution of gap states, as shown by the dotted line.

The simple cell structure discussed above suffers from the limitation that the cell efficiency is rather low (typically 8%). Use of light trapping within the cell by the use of a suitable back reflector (BR) can increase the efficiency to about 12%. The phenomenon of light-induced degradation, as discussed later, however, lowers this efficiency by about 50% when these high-efficiency single-junction cells are exposed to light. The highest-efficiency devices, therefore, use the multijunction approach in conjunction with a well-designed BR. Before we discuss the design considerations for these devices, we present below a discussion on light-induced degradation and its effect on cell performance.

6.08.4.3 Light-Induced Degradation

6.08.4.3.1 Amorphous silicon and silicon–germanium alloys

It was first reported by Staebler and Wronski (1977) that there are significant changes in the dark and photoconductivity of a-Si:H alloy films when subjected to light exposure. The phenomenon, named Staebler–Wronski effect (SWE) after the authors, is reversible. Annealing at temperatures around 150 °C for an hour restores the original values. The metastable changes in the material properties that take place under light exposure also have a pronounced effect on solar cell performance.

In the past 30 years, extensive work has been carried out both to obtain a fundamental understanding of light-induced degradation (LID) and to develop materials and devices that will be immune to this degradation. Although we have a much better understanding of this effect today, LID is always observed in high-quality materials and remains one of the most intensely investigated subjects (Fritzsche, 2001). Early work revealed several interesting features of this phenomenon:

1. The meta-stability is caused by changes in bulk properties. For example, the density of neutral-dangling bonds increases after light exposure.
2. Meta-stable defects can be created by charge injection, for example, by forward biasing a p–i–n diode in the dark.
3. Recombination of electron–hole pairs is necessary to trigger LID. A Schottky diode when

forward-biased does not show LID nor does a p–i–n junction when it is reverse-biased under illumination.

4. Exposure to light reduces cell efficiency. Maximum amount of degradation is in the FF. Degradation is more when the cell thickness is large. We should note that to absorb light efficiently, thick cells are needed, and these cells degrade the most.
5. Degradation does not go on indefinitely. As new defects are created, they also get annealed out so that equilibrium is reached after a few hundred hours. Degradation is less at high temperature.
6. Degradation is related to the microstructure and hydrogen bonding in the material (Guha *et al.*, 1992).

A typical plot of the degradation characteristic of a single-junction cell when exposed to light of one-sun intensity at 50 °C is shown in **Figure 9**. The cells are deposited on stainless steel with different i-layer thicknesses. It is clear that degradation is higher as the cell thickness increases. The highest stable efficiency is obtained for i-layer thickness of about 300 nm.

Degradation characteristic for a-SiGe alloy cells is also similar. A comparison of LID in an a-Si:H top cell and an a-SiGe:H bottom cell is shown in **Figure 10**. One can see that the a-SiGe:H bottom cell has degraded more than the a-Si:H top cell.

It has been proposed (Stutzmann *et al.*, 1985) that defects are created by nonradiative recombination of electron–hole pairs at spatially correlated tail states that correspond to the bonding and antibonding states of weak Si–Si bonds. The recombination releases about 1.5 eV energy that breaks a weak bond and generates a defect. To prevent the two neighboring bonds from recombining, a neighboring hydrogen atom moves in to separate the two dangling bonds. The defect pair may separate further by additional bond switching. In the annealing process, the hydrogen atoms revert back to their original positions. Hydrogen is thus directly involved both in the defect creation and in annealing.

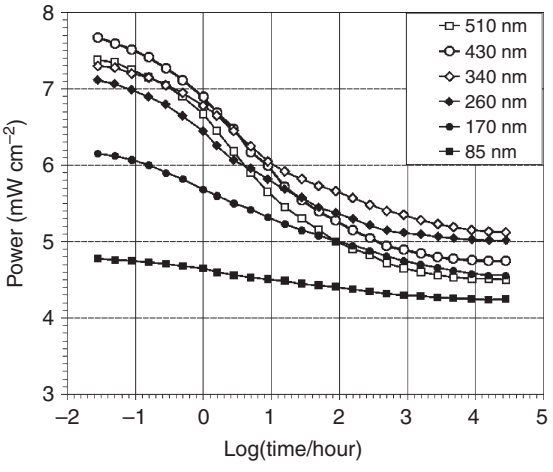

Figure 9 Kinetics of light-induced degradation of a-Si:H solar cells with different intrinsic layer thicknesses.

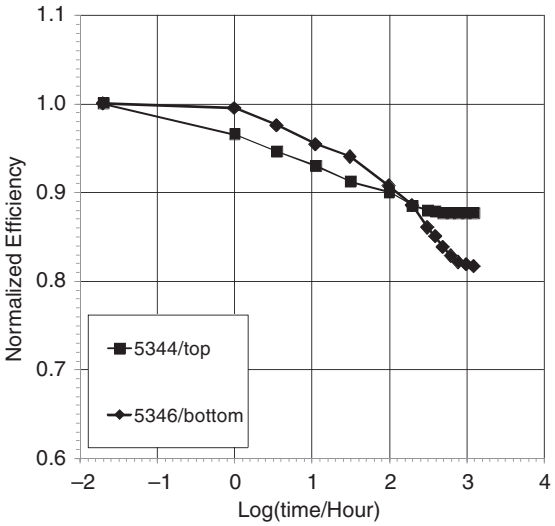

Figure 10 A comparison of light-induced degradations in an a-Si:H top cell (squares) and an a-SiGe:H bottom cell (diamonds).

There are still many open questions regarding the universal applicability of the above model. New models have been proposed (Branz, 1998; Biswas *et al.*, 1997), which attempt to explain the kinetics of both defect creation and annealing. Suffice is to say, there has not been a total consensus in the scientific community to quantitatively explain the various features of LID and annealing.

Hydrogen dilution (Guha *et al.*, 1981) seems to be the most effective method of improving LID. Since hydrogen dilution improves order in the material, and SWE is observed in amorphous materials only, it is reasonable to assume that hydrogen dilution will reduce SWE. Presence of excess hydrogen during growth also etches away the weak bonds, a potential cause for SWE. The presence of microcrystallites in the mixed-phase material has also been postulated to reduce SWE (Kamei *et al.*, 1999). It has been suggested that recombination events take place at the embedded crystallites where bonds are stronger and cannot be broken. We have also mentioned

previously the postulation that outside the microcrystallites, the amorphous matrix contains very little hydrogen. If SWE is related to presence of hydrogen in the material, the above suggests that even if recombination events take place in the amorphous region, SWE will be small.

Yan *et al.* (2001) have shown that the annealing of light-induced defects also is faster in the hydrogen-diluted alloys. Cells made with high hydrogen dilution show low activation energy of defect annealing and a narrow distribution of defect energy. This results in faster annealing of the light-induced defects in the edge material than in the conventional a-Si:H alloy, and contributes to lower LID. It is generally believed that both creation and annealing of these defects involve hydrogen motion. Measurements of diffusion coefficient of hydrogen in materials grown with different hydrogen dilution may help us to understand this mechanism better.

6.08.4.3.2 Nanocrystalline silicon

The nc-Si:H is an inhomogeneous material comprised of an amorphous phase, crystalline grains, and grain boundaries with a wide range of crystalline volume fraction. It also exhibits preferential orientation, and an anisotropic transport may be expected. Its meta-stability behavior, therefore, shows a substantial complexity and controversy, even more so than its a-Si:H counterpart. In some early studies, it was reported that no LID is observed in the nc-Si:H cells (Meier *et al.*, 1994; Yamamoto, 1999). Later on, it was found that certain nc-Si:H cells showed LID in their performance. Klein *et al.* (2003) reported that nearly no LID was observed in the nc-Si:H cell with the highest crystalline volume fraction, but cells with high amorphous volume fractions exhibit up to 10% degradation in the cell efficiency. For solar cells made at high deposition rate ($\sim$3.5 nm s^{-1}), Gordijn *et al.* (2005) demonstrated an improved solar cell performance after prolonged light soaking. They explained that the series resistance is reduced, and a new defect equilibration could be reached by light soaking.

In summary, LID in the nc-Si:H cells is much smaller than in the a-Si:H cells and some cells show undetectable changes after light soaking. Because LID in the nc-Si:H solar cells anneals away at an elevated temperature, the microscopic origin of the meta-stable structure changes in the nc-Si:H cells is similar to the conventional SWE, which is influenced by the presence of hydrogen in the material. In the nc-Si:H cells, hydrogen atoms are mainly located in the amorphous phase and the grain boundary region, and the hydrogen content in these regions is much higher than the conventional a-Si:H materials (Williamson, 2004, private communication; based on the flotation density analysis, the hydrogen content could be as high as 20–30 at.% in the amorphous and grain boundary regions). Therefore, it is logical to think that LID mainly occurs in the amorphous and grain boundary regions. However, the diphasic nature of the nc-Si:H cells not only results in many different meta-stable phenomena than those observed in the a-Si:H cells, but also makes any explanation for meta-stability in the nc-Si:H cells difficult.

Yan *et al.* (2004b) have systematically studied the spectrum dependence of LID in the nc-Si:H solar cells. As a comparison, the a-SiGe:H cells were also studied. **Figure 11** shows the normalized maximum power, $P_{max}(t)/P_{max}(0)$, as a function of light-soaking time for the nc-Si:H single-junction solar cells and the a-SiGe:H single-junction cells under red (>665 nm) light and blue (<650 nm) light, obtained from a solar simulator through long-pass and short-pass filters. For the nc-Si:H cell, the light intensities for the two spectra were adjusted to generate $J_{sc} \sim 44$ mA cm^{-2}, which is approximately 2 times the J_{sc} under AM1.5 illumination. For the a-SiGe:H cells, the light intensities were adjusted to generate $J_{sc} \sim 46$ mA cm^{-2} with the same consideration. The data clearly show that there is no LID for the nc-Si:H cell under red light, but some degradation

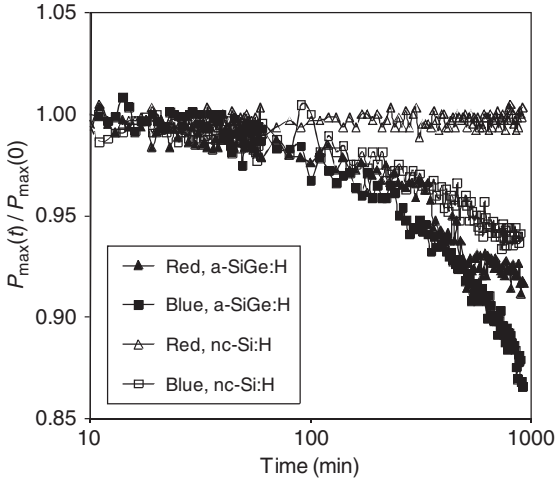

Figure 11 Light-soaking kinetics of the normalized efficiency of nc-Si:H single-junction solar cells and a-SiGe:H single-junction solar cells for different spectral regions.

under white light, and more degradation under blue light. Obviously, the absence of LID under red light illumination is due to the lack of absorption in the amorphous phase and no light-induced defect generation in the crystalline phase. In general, LID in the nc-Si:H is much less than that in the a-SiGe:H cell even under white light or blue light. These experiments confirm that the light-induced defect generation in amorphous phase and the grain boundary region is responsible for the degradation in the nc-Si:H solar cells. In addition, the light-induced changes can be annealed away at a high temperature for a prolonged time, indicating that the microscopic origin of LID in the nc-Si:H cells is similar to the conventional light-induced defect generation in the a-Si:H.

While nc-Si:H cells show very little degradation under forward bias, they are found to degrade under reverse bias. This is exactly opposite to the case for a-Si:H cells. Typical fractional change in FF as a function of electrical bias is shown. The results are explained in terms of a back-to-back diode model in which the diodes are considered to be formed at the interfaces of a-Si:H and nc-Si:H boundaries (Yue *et al.*, 2005a, 2005b).

6.08.4.4 Cell Performance

Hydrogen dilution has played a key role in obtaining the highest stabilized efficiency. Typical results for a-Si:H and a-SiGe:H alloy cells deposited on stainless steel are shown in **Table 2**. Both a-Si:H and a-SiGe:H alloy cells deposited using high hydrogen dilution not only show higher initial performance, but also maintain superior performance in the light-soaked state.

The optimum hydrogen dilution needed to obtain the best-quality component cell of a triple-junction structure depends on many factors. It is common to keep on increasing the hydrogen dilution till one sees a drop in V_{oc}, and then back off a little bit to get the best-quality material. An example of the effect of hydrogen dilution on the cell characteristic of a single-junction a-Si:H and a-SiGe:H cells are shown in **Tables 3** and **4**, respectively. Note the dramatic reduction in V_{oc} as the hydrogen dilution goes beyond the edge.

6.08.4.5 High Deposition Rate

High-rate deposition reduces the cost of thin-film solar panel production. However, it has been observed that the material quality and solar cell efficiency generally decrease with the increase of deposition rate. In the past decades, many research groups have put significant effort on high-rate deposition and explored various deposition methods and deposition parameter regimes. In this section, we describe the high-rate deposition issues and progresses.

6.08.4.5.1 High-rate a-Si:H and a-SiGe:H solar cells

Several deposition methods have been used for high-rate depositions of a-Si:H and a-SiGe:H solar cells, including the conventional rf glow discharge (Guha *et al.*, 1992), vhf glow discharge (Curtins *et al.*, 1987a, 1987b; Shah *et al.*, 1992; Yue *et al.*, 2007), microwave glow discharge (Guha *et al.*, 1994), HWCVD (Mahan *et al.*, 1991), thermal expansion PECVD (van de Sanden *et al.*, 1998), and others.

Table 2 Characteristics of a-Si:H and a-SiGe:H cells in both initial and degraded states

Description	*State*	J_{sc} *(mA cm*$^{-2}$*)*	V_{oc} *(V)*	*FF*	P_{max} *(mW cm*$^{-2}$*)*
300 °C, low dilution	Initial	12.3	0.94	0.65	7.5
	degraded	11.6	0.91	0.55	5.8
300 °C, high dilution	Initial	11.6	0.96	0.68	7.6
	degraded	11.2	0.94	0.61	6.4
175 °C, low dilution	Initial	11.4	0.96	0.64	7.0
	degraded	9.5	0.91	0.46	4.0
175 °C, high dilution	Initial	10.9	1.00	0.69	7.5
	degraded	10.5	0.97	0.60	6.1
a-SiGe, low dilution	Initial	17.6	0.72	0.55	7.1
	degraded	14.9	0.64	0.41	3.9
a-SiGe, high dilution	Initial	18.0	0.74	0.59	8.0
	degraded	16.3	0.69	0.45	5.1

Table 3 *J–V* characteristics of a-Si:H top cells on stainless steel with four different hydrogen dilutions measured under AM1.5 illumination

Hydrogen dilution	J_{sc} (mA cm^{-2})	V_{oc} (V)	*FF*	P_{max} (mW cm^{-2})
Near-optimum	10.04	1.018	0.732	7.48
Optimum	9.88	1.028	0.761	7.73
On-the-edge	9.82	0.624	0.426	2.61
Over-the-edge	8.95	0.459	0.562	2.31

Table 4 *J–V* characteristics of a-SiGe:H middle cells on stainless steel with four different hydrogen dilutions measured under AM1.5 illumination with a $\lambda > 530$ nm filter

Hydrogen dilution	J_{sc} (mA cm^{-2})	V_{oc} (V)	*FF*	P_{max} (mW cm^{-2})
Near-optimum	10.70	0.738	0.596	4.71
Optimum	10.60	0.756	0.654	5.24
On-the-edge	10.67	0.617	0.607	4.00
Over-the-edge	10.94	0.447	0.439	2.15

RF-deposited materials shows a clear increase of defect density (Guha *et al.*, 1992) and microvoid density (Williamson, 2003) as the deposition rate increases. As a result, the solar cell efficiency, especially the stable efficiency, decreases with the increase of the deposition rates. **Figure 12** shows an example of initial and stable solar cell efficiency as a function of deposition rates. One can see that the light-degraded efficiency drops more steeply than the initial efficiency.

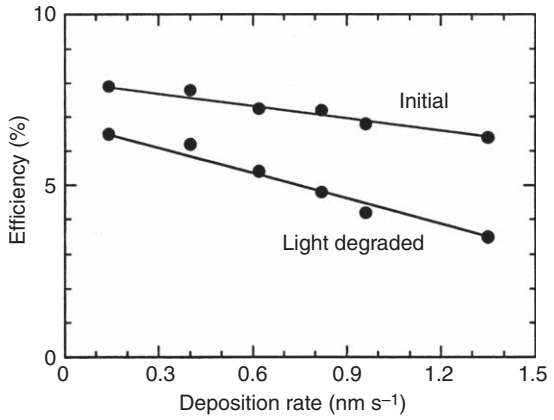

Figure 12 Initial and stable solar cell efficiency of a-Si:H solar cells deposited using conventional rf glow discharge at different rates. From Guha S, Yang J, Jones SJ, Chen Y, and Williamson DL (1992) Effect of microvoids on initial and light-degraded efficiencies of hydrogenated amorphous silicon alloy solar cells. *Applied Physics Letters* 61: 1444–1446.

In terms of the mechanisms of deterioration of material quality with deposition rates, three major effects have been identified. First, the high-rate deposited materials usually contain high dihydride and microvoid densities, which are responsible for the enhanced LID. The dihydrides are mainly caused by the SiH_2^* and SiH^* species in the plasma, which are generated by high-energy electrons. Because the density of high-energy electrons increases with the increase of RF power, an effective and commonly used way to increase the deposition rates, the high-rate RF-deposited a-Si:H and a-SiGe:H solar cells show poorer efficiency than that for the low-rate deposited solar cells. Second, the ion energy increases with the increase of RF power, and high-energy ion bombardment is also believed to cause material degradation. Finally, during high-rate deposition, the impinging species do not have sufficient time on the growth surface to move and find favorable locations with low energy to form compact and low-defect structures. This results in poorer material.

The vhf glow discharge showed significant advantages to obtain high material quality at high deposition rates (Curtins *et al.*, 1987a, 1987b; Shah *et al.*, 1992; Yue *et al.*, 2007). The deposition rate increases with the excitation frequency. In principle, one can obtain high-rate deposition with increased frequency without increasing the excitation power density. In this case, the electron temperature does not increase and the densities of

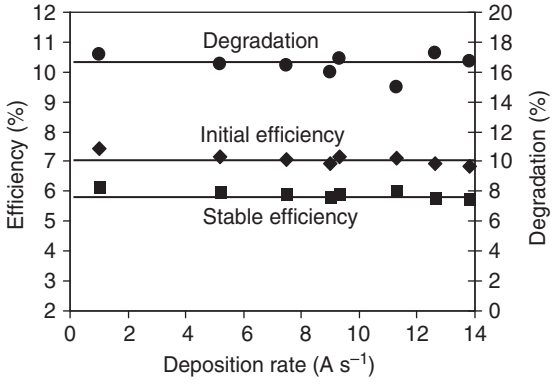

Figure 13 Deposition rate dependence of initial and stable efficiencies as well as the light-induced degradation of a-Si:H solar cells deposited with a modified vhf glow discharge. From Yue G, Yan B, Yang J, and Guha S (2007) High rate deposition of amorphous silicon based solar cells using modified very high frequency glow discharge. *Materials Research Society Symposium Proceedings* 989: 359–364.

SiH_2^* and SiH^* in the plasma are not increased dramatically with deposition rates. Moreover, the high frequency reduces the ion energy and increases the ion flux intensity. The lower-energy and high-flux ion bombardments do not damage the growth surface but enhance the surface mobility of impinging species. The combination of these effects results in a much lower sensitivity of a-Si:H and a-SiGe:H properties on the deposition rates. **Figure 13** shows the deposition rate dependence of initial and stable efficiency, as well as the ratio of LID, in a-Si:H solar cells deposited with a modified vhf glow discharge (Yue *et al.*, 2007). One can see that both the initial and the stable efficiencies do not show a clear correlation to the deposition rate up to $\sim$14 Å s^{-1}. The a-SiGe:H materials and solar cells deposited with vhf at high rates also show superior properties over the RF-deposited high-rate materials. With high-rate a-Si:H and a-SiGe:H deposited materials for triple-junction cells, initial and stable cell efficiencies of 11.3% and 10.1% have been achieved using vhf-deposited intrinsic layers, where the deposition time was less than 50% of the current corresponding deposition time in the production lines.

Microwave glow discharge has also been demonstrated as an effective method for high-rate depositions of a-Si:H and a-SiGe:H solar cells. Guha *et al.* (1994) showed that high-efficiency a-Si:H and a-SiGe:H cells can be deposited at deposition rates up to 100 Å s^{-1}. However, although the initial cell efficiency was reasonably good, the LID was very high. SAXS measurement showed that the microvoid density was high in the microwave-deposited materials (Guha *et al.*, 1994; Williamson, 2003).

HWCVD is another method to demonstrate high deposition rate of a-Si:H and a-SiGe:H materials. The deposition rate can be increased to 100 Å s^{-1}. However, reasonable cell efficiency was only achieved with a deposition rate around 10 Å s^{-1} (Mahan *et al.*, 1998). In addition, some large-area issues and wire lifetime issues have delayed the use of HWCVD in large-scale solar panel production. In recent years, the thermal expansion glow discharge showed some promising results on high-rate a-Si:H solar cells. However, no high-efficiency solar cells have been demonstrated with this method (van de Sanden *et al.*, 1998).

6.08.4.5.2 High-rate nc-Si:H solar cells

In order to employ nc-Si:H in solar panel manufacturing, the deposition rate has to be high enough such that the total deposition time is comparable to the current a-Si:H- and a-SiGe:H-based solar cell deposition. Normally, an a-Si:H solar cell has an intrinsic layer about 200–300 nm, while an nc-Si:H solar cell needs at least 1- to 2-μm-thick intrinsic layer. Therefore the deposition rate of nc-Si:H should be at least a factor of 5 higher than the a-Si:H deposition. In reality, researchers target the deposition rate at >10 Å s^{-1}. In order to achieve such high deposition rates, various deposition methods have been explored (Shah *et al.*, 2003; Yan *et al.*, 2003a, 2003b). The most successful method is the vhf glow discharge (Shah *et al.*, 2003; Yan *et al.*, 2003b).

A second approach for high-rate nc-Si:H solar cells is RF glow discharge in a high-pressure and high-power-depleting regime (Kondo, 2003; Guo *et al.*, 1998; Fukawa *et al.*, 2001). Guo *et al.* initially proposed this method and demonstrated a significant advantage in high-rate deposition of nc-Si:H films in this regime. Although the mechanism of improving nc-Si:H properties using the high-power, high-pressure, and depleting regime may not be understood very well, a simplified explanation could be summarized as follows. High-rate deposition needs a high-power density. In order to avoid the high ion bombardment in the high-power regime, a high pressure is used to enhance the collisions of ions during their traveling in the plasma sheet and reduce the ion energy. In addition, in the depleting conditions, a significant amount of atomic

hydrogen is generated from the decomposition of SiH_4, which reduces the required hydrogen dilution ratio for amorphous to nanocrystalline transition. Based on the Paschen curve, a high pressure needs a smaller spacing between the cathode and anode. Therefore, the deposition in the high-pressure, high-power, and depleting regime needs a narrow spacing. Currently, most groups use spacing between 4 and 12 mm.

The most attractive approach is the combination of vhf and the high-power, high-pressure, depleting regime. In this case, the advantages of these two approaches are added together. Kondo and his colleagues in AIST have systematically studied the nc-Si:H material properties as a function of various deposition parameters in the high-power, high-pressure, and depleting regime. In addition, they also investigated the possibility of using a mesh electrode between the cathode and the substrate to control the ion energy and reduce the ion bombardment. Recently, Kondo *et al.* used vhf at the high-pressure, high-power, depleting regime and improved their nc-Si:H cell efficiency significantly. They reported an efficiency of 9.4% with an nc-Si:H single-junction solar cell deposited at 15 Å s^{-1} and 9.1% at 23 Å s^{-1} (Kondo *et al.*, 2005).

As mentioned earlier, LID in single-junction cell limits their applicability, and multijunction cell structures are usually used to obtain high stable efficiency.

6.08.5 Multijunction Cell

6.08.5.1 Basic Structure

LID limits the efficiency of single-junction cells, and multijunction cell structures are usually designed to increase stable cell efficiency. Use of thinner intrinsic layers improves stability and incorporation of different band-gap i-layers increases the efficiency. Although any number of cells can be stacked together to form the multijunction structure, from a practical point of view, the losses in the junction between the cells and the problem with current matching of the component cells limit the maximum number that can be used without affecting the efficiency. Both double- and triple-junction cell structures have been extensively used, and the highest cell efficiency has been reported with the latter.

The triple-junction structure shown in **Figure 14** has demonstrated the highest stable cell efficiency of 13% (Yang *et al.*, 1997, 2003). Light enters from the top, and the thin layer (60 nm) of ITO serves as the antireflection coating and also forms a low-resistance contact to the top doped layer. Typical sheet resistivity of ITO is 50–100 Ω/square, and silver grid lines are evaporated on this layer to reduce series resistance losses. The three-component p–i–n cells use i-layers of different band gaps. The top cell has an optical gap of about 1.8 eV and captures the blue light. The intrinsic layer of the middle cell incorporates about 10% Ge to lower the gap to about 1.6 eV.

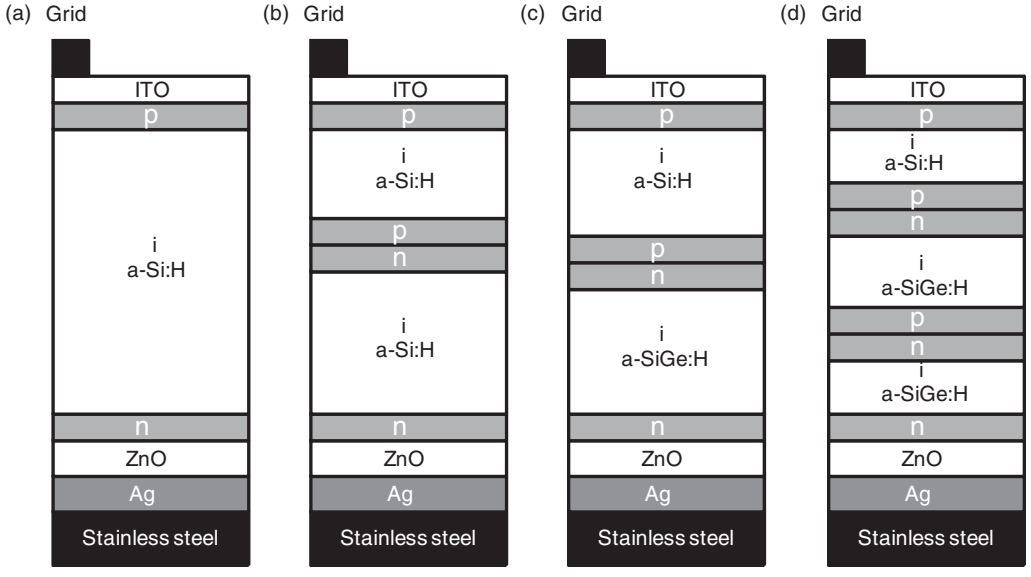

Figure 14 Various substrate-type a-Si:H and a-SiGe:H solar cell structures. (a) Single junction, (b) same-gap double junction, (c) dual-gap double junction, and (d) triple junction.

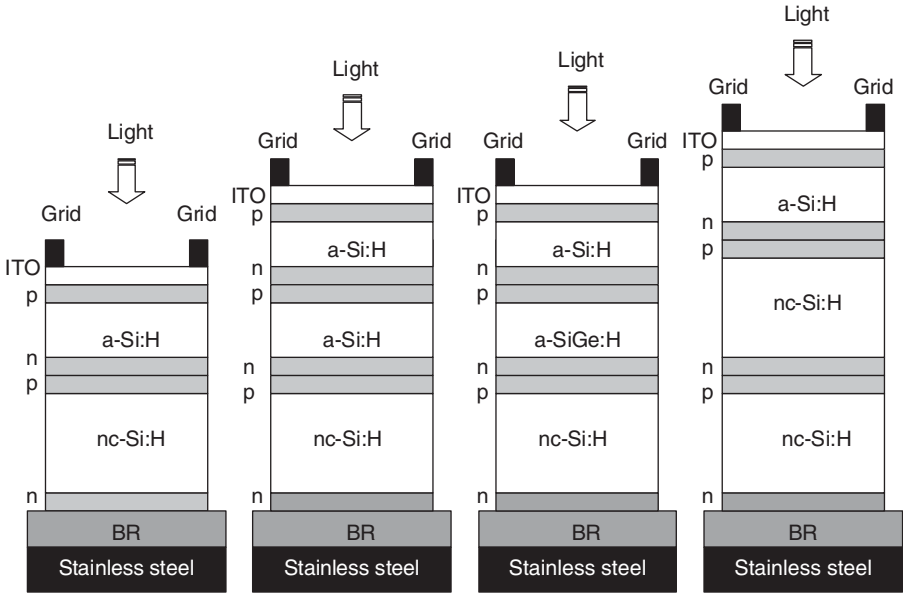

Figure 15 Various substrate-type solar cells incorporating nc-Si:H.

This cell captures the green photons. The i-layer of the bottom cell has about 40% Ge and has a gap of about 1.4 eV. This captures the red light. The longer-wavelength photons that are not absorbed get reflected from the BR that consists of a bilayer of silver and zinc oxide. The BR usually is textured so that the light is reflected at an angle to facilitate multiple reflections.

An nc-Si:H has also been used successfully in multijunction cells to replace either the bottom layer or both the bottom and the middle layers. Typical cell structures are shown in **Figure 15**. The highest stable cell efficiency of 13.3% has been achieved with an a-Si:H/nc-Si:H/nc-Si:H structure (Yan *et al.*, 2006).

6.08.5.2 Key Requirements for Obtaining High Efficiency

In order to obtain high efficiency in a multijunction cell structure, the following are the requirements: (1) high-quality BR for efficient light trapping, (2) doped layers with high conductivity and low optical loss, (3) high-quality intrinsic layers of different band gaps, (4) high-quality component cells with proper current matching, (5) low-resistance tunnel junctions, and (6) antireflection coating or window layer of high conductivity and transparency. We give below a discussion on how these different requirements can be fulfilled.

6.08.5.2.1 BR for light trapping

Multiple passes within the cell using suitable BR increase the optical path and improve photon absorption especially for the long-wavelength photons. Yablonovitch and Cody (1982) and Yablonovitch (1982) have shown that for random scattering, the path length can be increased by a factor of $4n^2$ where n is the refractive index of the material. For a-Si:H alloy, this amounts to about 50 passes or 25 reflections. **Figure 16** shows the calculated value of the fraction of absorbed light as a function of wavelength for different number of internal reflections (Banerjee and Guha 1991; Banerjee *et al.*, 1994b). The calculation assumes an a-Si:H solar cell with an optical gap

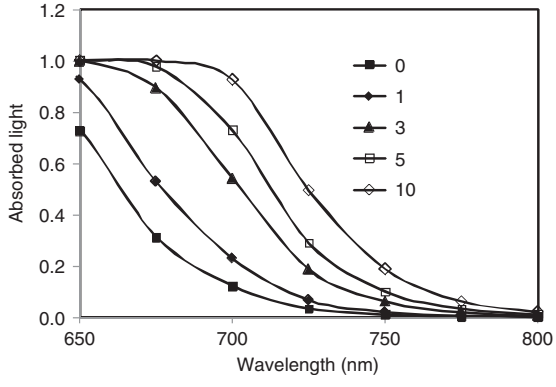

Figure 16 Light absorbed in a-Si:H solar cell as a function of wavelength for different number of reflections.

of 1.68 eV and i-layer thickness of 500 nm. The series of curves show the significant enhancement in photon absorption that can be obtained in the red/infrared part of the spectrum with an increasing number of reflections within the cell.

For a cell with a superstrate structure, light trapping is achieved through the use of textured tin oxide on glass. Asahi glass has been extensively used that allows the light to enter the cell at an oblique angle. The BR is usually a bilayer of ZnO and Ag. The layer of ZnO in this case prevents tarnishing of the silver that takes place when in contact with the silicon layer.

For the substrate structure, again a bilayer of Ag and ZnO is used. The silver can be textured by sputtering at a high temperature. In some cases, ZnO is also textured either by depositing at a high temperature or by subsequent etching. A schematic diagram of a textured BR and resultant light scattering is shown in **Figure 17**. The amount of texture is critical to obtain optimum light trapping (Banerjee and Guha, 1991; Banerjee *et al.*, 1994b).

Figure 18 shows four AFM pictures of BRs made under various conditions and chemical treatments, where (a) is for a conventional BR (R1748) developed previously (Banerjee and Guha, 1991; Banerjee *et al.*, 1994b), (b) is for a BR (R7900) with large microfeatures created by adjusting the deposition parameters, (c) is for a BR (R7948) with a thicker ZnO before chemical etching, and (d) is for the same BR as in (c) but after 30-s chemical etching in 0.5% HCl (Yan *et al.*, 2005).

The microfeature size on the conventional BR is on the order of 0.1–0.2 μm with a root mean square (RMS) roughness of 38.2 nm. By adjusting the deposition parameters, one can increase the feature size to as large as 0.5–1.0 μm with an RMS of 80.5 nm (**Figure 18(b)**). In addition, the chemical etching modifies the microfeatures on the BR surface. It seems that the small features are etched away and the feature size effectively increases. Correspondingly, the RMS increases from 39.6 to 63.2 nm after 30-s etching in 0.5% HCl, as shown by comparing **Figures 18(c)** and **18(d)**. It clearly shows that RMS roughness increases after the chemical etching.

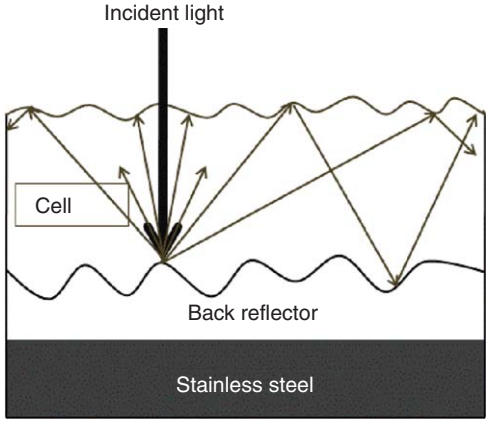

Figure 17 Schematic of light trapping.

In order to confirm that the enhanced texture indeed results in high current in solar cells, **Figure 19** shows a comparison of QE curves on the a-SiGe:H solar cells on Ag/ZnO BRs with different textures. The results show that the extra texture removes the interference fringes and increases the total current by 1 mA cm^{-2} for this type of solar cells.

The light trapping effect has also been investigated in the nc-Si:H solar cells. **Figure 20** shows the QE curves of the four nc-Si:H solar cells. Similar to the a-SiGe:H solar cells, the increase of microfeature size eliminates the interference fringes from the QE curves, indicating diffuse scattering in the devices. The difference to the a-SiGe:H cells is a clear gain in the J_{sc} obtained by increasing the roughness on the BR surface. The interpretation for the difference in the two cases could be as follows: the intrinsic layer in the nc-Si:H cells is over 1-μm thick, which is a few times larger than the relevant wavelength of the light in the spectrum (taking the wavelength compression factor into account). The light scattered at small angles θ may reach the condition of total internal reflection at the semiconductor/ITO interface or the ITO/air interface, and hence the light can be trapped in the semiconductor layers with multiple passes. In addition, the growth of nc-Si:H also produces extra features on the surface as previously observed (Yan *et al.*, 2004c, 2004d). The growth of nc-Si:H is not conformal with the substrate morphology due to the increase of texture during the nc-Si:H growth. Therefore, light trapping can be effectively achieved by large microfeatures on the substrate.

Theoretically, the best BR is with a flat Ag and textured ZnO because the flat Ag reduces the plasmon loss at the Ag/ZnO interface and the textured ZnO provides the required light scattering (Sopori *et al.*, 1999; Hegedus *et al.*, 2002). Yan *et al.* (2008a) have shown that this is the case for the ZnO thicker than 2 μm. With a thinner ZnO layer, a textured Ag is still necessary because the light scattering is not sufficient at the ZnO/a-Si:H interface.

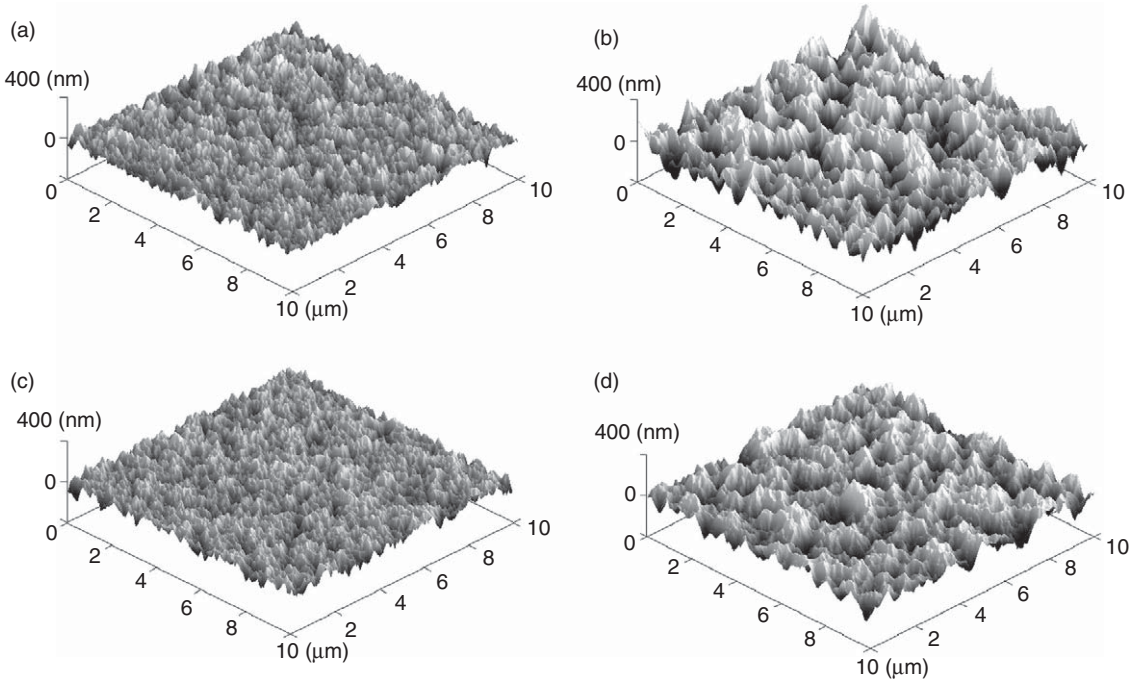

Figure 18 AFM pictures of four Ag/ZnO BRs made with various deposition and chemical etching parameters. From Yan B, Owens, JM, Jiang C-S, Yang J, and Guha S (2005) Improved back reflector for high efficiency hydrogenated amorphous and nanocrystalline silicon-based solar cells. *Materials Research Society Symposium Proceedings* 862: 603–608.

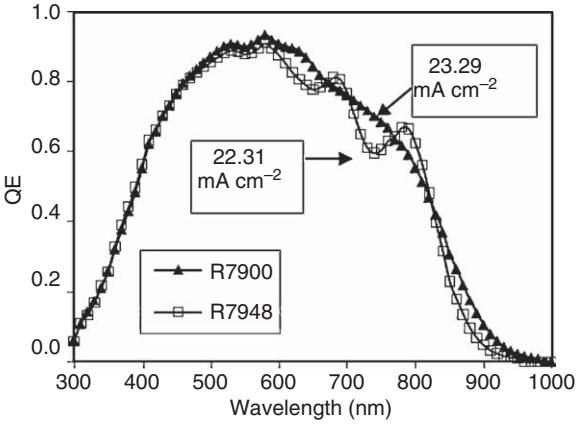

Figure 19 QE curves for a-SiGe:H solar cells on Ag/ZnO BR having less texture (R7948) and more texture (R7900). From Yan B, Owens JM, Jiang C-S, Yang J, and Guha S (2005) Improved back reflector for high efficiency hydrogenated amorphous and nanocrystalline silicon-based solar cells. *Materials Research Society Symposium Proceedings* 862: 603–608.

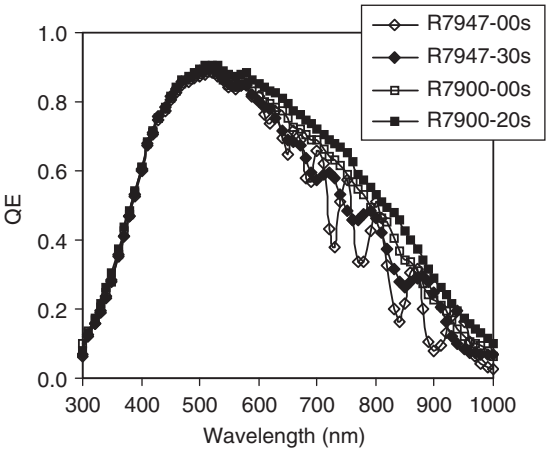

Figure 20 QE curves for nc-Si:H solar cells on Ag/ZnO BR having less initial texture (R7947) and more initial texture (R7900), and after HCl etching. From Yan B, Owens JM, Jiang C-S, Yang J, and Guha S (2005) Improved back reflector for high efficiency hydrogenated amorphous and nanocrystalline silicon-based solar cells. *Materials Research Society Symposium Proceedings* 862: 603–608.

Many new methods of efficient light trapping are now being explored. They include the use of optical confinement by a grating structure (Haase and Stiebig, 2006), nanoparticles (Pillai *et al.*, 2007), and photonic structures (Zhou and Biswas, 2008). Comprehensive reviews can be found in the literature (Schropp and Zeman, 1998; Krc *et al.*, 2006).

6.08.5.2.2 Doped layers

The doped layers in the cell serve the purpose of providing low-resistance contacts to the conducting oxide layers and also to each other in between the junctions. High electrical conductivity is a requirement to perform these functions. Moreover, in order to obtain high V_{oc}, it is necessary that the doped layers should have low electrical activation energy, which also requires that the doped layers should be highly conducting. Another requirement for the doped layer is transparency to light. Since the doped layers are inactive in the PV process, light absorbed in these layers does not contribute to photocurrent. In order to obtain high efficiency with single- or multijunction devices, high band gap, high electrical conductivity materials with low optical loss are necessary.

Use of phosphorus doping can produce an n-type layer with high conductivity. Films with electrical conductivity of 10^{-2} $(\Omega/\text{square cm})^{-1}$ with an activation energy of 100 meV can be easily obtained by mixing phosphine with silane in the gas stream. Boron-doping in the a-Si:H alloy is not as successful in moving the Fermi level close to the band edge because of the high defect density associated with the valence band tail. The best conductivity is only around 10^{-4} $(\Omega/\text{square cm})^{-1}$ with an activation energy of 300–400 meV. Moreover, incorporation of B results in lowering of the gap of a-Si:H alloy, resulting in a higher optical absorption in the material. Solar cells made with p-type a-Si:H alloy as the doped layer are thus characterized by low V_{oc} and $\mathcal{J}_{sc}$. There have been two main approaches to alleviate the above problem. One is to incorporate carbon to widen the band gap. In the other approach, microcrystalline alloys are used. Both the approaches are used extensively to make high-efficiency devices.

Incorporation of C in the film increases the band gap of the material. Boron doping lowers the band gap, and to obtain p-type amorphous silicon carbon (a-SiC:H) alloy of about 2 eV band gap, a carbon concentration of 30–40% is needed (Tawada *et al.*, 1982). Incorporation of such a large quantity of C increases the defect density in the material and makes doping efficiency poorer. The conductivity of the material is lower than 10^{-6} $(\Omega/\text{square cm})^{-1}$, and the activation energy is about 0.5 eV. This poses a problem in obtaining low-resistance contact to the conducting oxide layers and also to the adjacent n-layers in the multijunction. Boron-doped a-SiC:H alloy films, as the window layer through which light first enters, have been used in many laboratories (Catalano, 1991) to obtain single-junction devices with high V_{oc} and $\mathcal{J}_{sc}$. QE at 400 nm has been demonstrated to exceed 60% (Catalano and Wood, 1988), indicating low absorption in the p-layer.

Doped microcrystalline silicon alloys are characterized by low optical absorption and high conductivity. Guha *et al.* (1986) demonstrated that thin layers of microcrystalline p-type materials can be made showing high conductivity and low optical loss. The alloy was grown using a very dilute mixture of silane in hydrogen at a higher power density than is normally used for growing a-Si:H alloy. We have discussed before the use of a heavy dilution of hydrogen to facilitate grain growth to obtain microcrystalline material. Both diborane and boron trifluoride were used as the dopant gas and were used to make high-efficiency single- and multijunction devices. Incorporation of microcrystalline p-layers in single-junction cells has resulted in V_{oc} greater than 1 V and QE at 400 nm exceeding 75%. This has also resulted in very low resistance at the tunnel junctions between the component cells. These results will be discussed later.

A natural extension of this work is to grow microcrystalline SiC:H layers. Such layers have been made in several laboratories (Guha and Kulman, 1986; Hattori *et al.*, 1987; Goldstein *et al.*, 1988). Although high V_{oc} has been demonstrated using this alloy (Guha and Kulman, 1986), studies involving incorporation of these materials in cells are rather limited. In contrast to the p-type layer, microcrystalline n-layers are easier to grow, and both fluorinated and nonfluorinated n-type layers have been made (Tsu *et al.*, 1981; Nakatani *et al.*, 1983). As we have discussed before, V_{oc} of the cell is primarily determined by the major junction (Pawlikiewicz and Guha, 1990), and use of the microcrystalline n-layer does not increase V_{oc}. The optical loss, however, is lower, and, recently, microcrystalline n-layer has been used successfully to obtain high-efficiency multijunction devices (Yang *et al.*, 1997, 2003).

6.08.5.2.3 Intrinsic layers

- *High-band-gap alloys for the top cell.* In order to capture the blue light of the solar spectrum, it is necessary to use i-layers with an optical gap greater than 1.8 eV. There are two main approaches to obtain the higher band gap. The first approach uses a-SiC:H alloy (Li, 1993; Yoshida *et al.*, 2000; Nomoto *et al.*, 1989). In the second approach, an a-Si:H alloy deposited at low temperature and high hydrogen dilution is used (Kamei *et al.*, 1996; Hanaki *et al.*, 1989; Yang *et al.*, 1994, 1996; Guha *et al.*, 1994, 1996).

We have mentioned before that addition of carbon-containing feedstock gases to silane can increase the band gap of the alloy. Introduction of C, however, introduces new states in the gap and makes the transport properties poorer. The large amount of LID associated with thicker cells made from a-SiC:H alloy makes this material impractical for use in designing high-efficiency cells unless dramatic improvement in material properties are made.

The second approach for making the top cell is to use hydrogen-diluted a-Si:H alloy deposited at a low temperature for the i-layer and microcrystalline silicon alloy for the p-layer. By increasing the hydrogen dilution, the top cell with V_{oc} of 1.054 V with an FF of 0.76 has been reported (Yang *et al.*, 1996).

High-band-gap alloys have also been made by incorporating oxygen or nitrogen in the alloy; the minority transport properties are, however, poor, and solar cell results are not available (Williams *et al.*, 1993).

- *Low-band-gap alloys for middle and bottom cells.* The middle and the bottom cells need to absorb the green and the red photons, and the band gap of the i-layer needs to be lower than what is typically obtained for an a-Si:H alloy (1.7–1.8 eV). Addition of germane to the gas mixture can continuously change the band gap from 1.7 to 1.1 eV. The a-SiGe:H alloys are, therefore, used extensively for the middle and the bottom cells.

The most commonly used active gases are silane and germane. These two gases have very different dissociation rates in the plasma. This causes deterioration in the material quality and also compositional nonuniformity along the direction of the gas flow. While high hydrogen dilution can improve the film quality, the problem of nonuniformity in the deposition remains. Guha *et al.* (1987) have used a mixture of disilane and germane to deposit the a-SiGe:H alloy. Since disilane and germane have similar dissociation rates in the plasma, the problem of compositional inhomogeneity is significantly reduced. Both disilane and germane are easily dissociated in the plasma and in order to eliminate powder formation and to reduce deposition rate under normal plasma conditions, hydrogen is used as a diluent. Although the film properties improve remarkably when deposited from a gas mixture of disilane and germane diluted in hydrogen, they are still poorer than those of an a-Si:H alloy only. There are many reasons for this. The compositional disorder in the a-SiGe:H alloy makes the conduction band tail wider (Aijishi *et al.*, 1989; Wang *et al.*, 1993). The microstructure is also poorer (Williamson, 1995), probably due to lower adatom mobility of GeH_3 molecules. Although significant advances have been made in improving the material properties of a-SiGe:H alloys (Aijishi *et al.*, 1989), there is almost a continuous degradation of transport properties as the Ge content in the alloy is increased. Cells incorporating the a-SiGe:H alloy in the i-layer thus have a poorer FF than the corresponding a-Si:H alloy cell.

A novel way of improving the efficiency of a-SiGe:H alloy cells was reported by Guha *et al.* (1989) by profiling the composition of a-SiGe:H alloy throughout the bulk of the intrinsic material so as to have a built-in electrical field in a substantial portion of the intrinsic material. Different types of profiling configurations are shown in **Figure 21**. Two simple cases were considered first: (1) the band

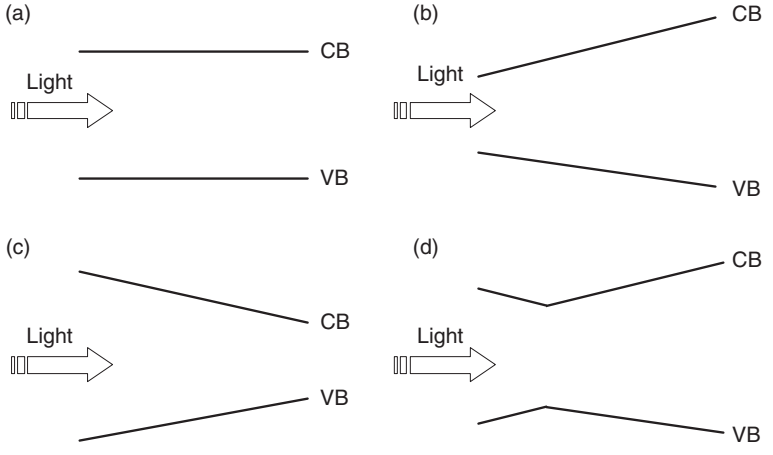

Figure 21 Different types of profiling configurations for a-SiGe:H solar cells.

gap is minimum at the p–i interface through which light enters and increases linearly away from the interface (normal profiling) and (2) the band gap is maximum at the p–i interface and decreases away from it (reverse profiling). From band structure considerations, assuming that both the conduction and the valence band edge positions shift equally as Ge is incorporated in the material, intuitively one would expect that normal profiling will help the hole transport and make the electron transport more difficult. The opposite will be the case for reverse profiling. Since hole transport is the limiting factor determining a-Si:H alloy solar cell performance, one would therefore expect an improvement in the FF for the case of normal profiling. Note that in this case, the maximum number of carriers is generated right at the p–i interface and the holes have a very short distance to move. However, since the open-circuit voltage of the solar cell is determined by the major junction that is at the p–i interface, one expects a higher open-circuit voltage for the reverse profiling, where the band gap for the i-layer at the p–i interface is larger.

Experimental results for V_{oc}, FF, and J_{sc} for the three structures with no profiling, normal profiling, and reverse profiling are shown in **Table 5**. The results are for red-light illumination. As theoretically predicted (Guha *et al.*, 1989; Zimmer *et al.*, 1998; Rubinelli *et al.*, 2002), normal profiling is seen to give better FF, and reverse profiling gives higher open-circuit voltage.

The highest efficiency devices for the middle and the bottom cells use a double-profiled a-SiGe:H alloy in the i-layer, as shown in **Figure 21**(**d**). Several groups (Nakata *et al.*, 1990; Zimmer *et al.*, 1997; Dalal and Baldwin, 1993) have used this method to design high-efficiency cells. The middle cells typically use 1.6-eV band gap material at the minimum position. For the bottom cell, the corresponding band gap is ~1.4 eV.

Table 5 Experimental results for a-SiGe alloy cells with different types of profiling[a]

	Constant band gap 1.55 eV	*Normal profiling 1.45–1.72 eV*	*Reverse profiling 1.72–1.45 eV*
J_{sc} (mA cm^{-2})	3.43	3.68	3.48
V_{oc} (V)	0.73	0.68	0.74
FF	0.57	0.68	0.37
Power (mW cm^{-2})	1.43	1.72	0.93

[a] The results are for red-light illumination.

The highest initial efficiency of a-SiGe:H alloy cells, where the i-layer uses an alloy with Ge content suitable for the middle cell, is shown in **Figure 22** (top). The efficiency under AM1.5 illumination is 10.84%. When an alloy of Ge content suitable for the bottom cell is used, the highest initial efficiency is 10.37% (**Figure 22** (bottom)). The high level of Ge in the i-layer results in a QE of 45% at 850 nm, indicating excellent red-response characteristic (Yang *et al.*, 1994).

- *nc-Si:H intrinsic layer.* Since the early report of an nc-Si:H solar cell in 1994 (Meier *et al.*, 1994), several important innovations have been made by researchers around the world. First, the reduction of impurity in nc-Si:H has improved the quality of the

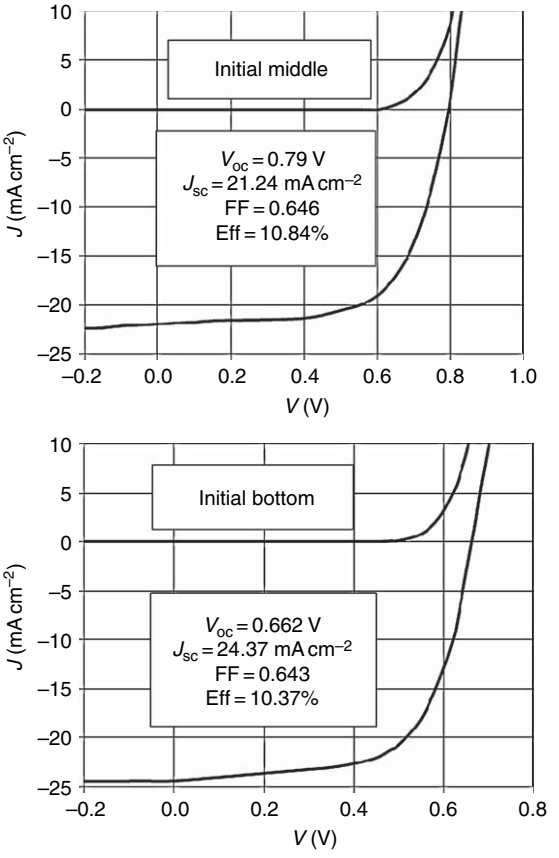

Figure 22 The highest initial efficiency of a-SiGe:H solar cells where the i-layer uses an a-SiGe:H film with Ge content suitable for the middle (top) and bottom (bottom) cells in an a-Si:H/a-SiGe:H/a-SiGe:H triple-junction structure. From Yang J, Banerjee A, Glatfelter T, Hoffman K, Xu X, and Guha S (1994) Progress in triple-junction amorphous silicon-based alloy solar cells and modules using hydrogen dilution. In: *First World Conference on Photovoltaic Energy Conversion Proceedings*, p. 380. New York: IEEE.

material to be acceptable for high-efficiency solar cells. Second, the porosity of nc-Si:H has been reduced significantly, which resolves the issue of ambient degradation. Third, a hydrogen dilution profiling technique was developed to control the nanocrystalline evolution, under which condition the nc-Si:H films showed uniform crystallinity along the growth direction. Fourth, nc-Si:H solar cell design has been optimized especially near the interface layer. The combination of all the techniques has resulted in attaining high efficiency in multijunction solar cells incorporating nc-Si:H.

1. *Impurity reduction.* As mentioned before, oxygen acts as a dopant in nc-Si:H, and affects material quality even at levels that can be tolerated in a-Si:H. Shah and his colleagues systematically studied the oxygen contamination effect on nc-Si:H properties and explored different ways to reduce the oxygen content in nc-Si:H (Kroll *et al.*, 1995). First, they used microdoping to compensate the n-type doping from oxygen impurity. This method can effectively control the conductivity activation energy to move the Fermi level to the middle of the band gap. However, the window of the proper doping levels is very narrow, and it is difficult to control precisely. Second, they tried to reduce the degassing from the chamber and use gas purifiers in the gas line to reduce the impurity levels. **Table 6** lists the oxygen levels in nc-Si:H films deposited under various deposition conditions. The results showed that the oxygen impurity came from both the degassing and the process gases. Reducing the degassing from the chamber wall is a critical factor for reducing the impurity level. Using a gas purifier also reduces the impurity level if the degassing rate is low enough.

Nasuno *et al.* (2000) found that the oxygen impurity is not electronically active when the deposition temperature is low. They demonstrated an nc-Si:H solar cell efficiency of 9.4% deposited at 140 °C without gas purification. In these conditions, the oxygen impurity level in the nc-Si:H intrinsic layer is $\sim 2 \times 10^{19}$ at. cm^{-3}.

Table 6 Oxygen content in nc-Si:H films deposited under different degassing rates and with or without gas purifiers

Degassing rate (mbar l s^{-1})	*Gas purifier*	*O content (at. cm^{-3})*
6.4×10^{-6}	Yes	3.5×10^{20}
1.7×10^{-6}	No	4.0×10^{19}
	Yes	6.0×10^{18}
8.5×10^{-7}	Yes	2.0×10^{18}

2. *Compactness and ambient degradation in the nc-Si:H solar cells.* The material structure in nc-Si:H contains a cluster of nanometer-sized grains and amorphous tissue. The inhomogeneous material structure makes nc-Si:H materials easily having a high microvoid or microcrack density. For nonoptimized nc-Si:H films, the microvoid density can be as high as 3% in the volume fraction (Williamson, 2003). The high microvoid density causes postdeposition impurity diffusion. The major problem associated with the impurity diffusion is an ambient degradation of the nc-Si:H solar cell efficiency without intentional light soaking (Yan *et al.*, 2002). The high porosity in the nc-Si:H materials is normally associated with a high crystalline volume fraction and large grain sizes. It has been reported that the best nc-Si:H solar cells were made close to the amorphous/nanocrystalline transition but on the nanocrystalline side. The major advantage is that the materials deposited close to the transition region have a more compact structure than those with high crystallinity. The high-quality nc-Si:H materials show a microvoid density less than 0.3% in the volume fraction (Williamson, 2004, private communication), which is about one order of magnitude lower than previously reported (Williamson, 2003).

3. *Hydrogen dilution profiling.* It has been reported that the transition from amorphous to nanocrystalline phases depends on the hydrogen dilution in the process gases and the thickness of the films. The crystalline volume fraction normally increases with the film thickness. This phenomenon is called nanocrystalline evolution. **Figure 23** shows a cross-sectional TEM image of an nc-Si:H film made with a hydrogen dilution ratio $R = 20$ (H_2/SiH_4) (Collins *et al.*, 2003). Three observations can be summarized from this figure. First, there is an amorphous incubation layer; second, nucleation happens with a uniform nucleation density; third, after the nucleation, cone-shaped nanocrystalline clusters grow with the film thickness until the nanocrystalline cones collide.

The material structure, as shown in **Figure 23**, has a significant impact on the nc-Si:H cell performance. First, the a-Si:H incubation layer adds a significant series resistance to the cell's *J–V* characteristics because of the low photoconductivity (low carrier mobility); second, the enhanced crystallinity at the region near the top surface results in poorer grain boundary passivation and a high

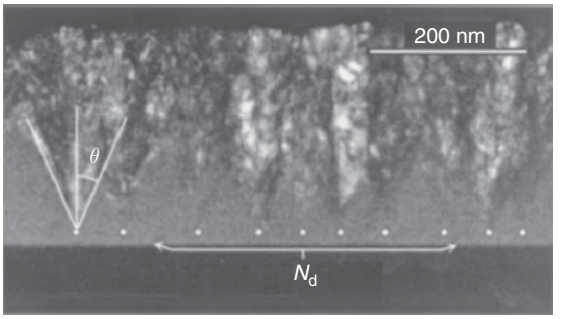

Figure 23 Cross-sectional TEM image of a nc-Si:H with $R = 20$. A representative conical nanocrystalline structure is indicated, and the points near the substrate interface identify the nuclei, where N_d denotes the density of nuclei. From Collins RW, Ferlauto AS, Ferreira GM, *et al*. (2003) Evolution of microstructure and phase in amorphous, protocrystalline, and microcrystalline silicon studied by real time spectroscopic ellipsometry. *Solar Energy Materials and Solar Cells* 78: 143–180.

density of microvoids and microcracks. In order to achieve improved material quality along the growth direction, Yan *et al.* (2004c, 2004d) have developed a hydrogen dilution profiling method to control the nanocrystalline evolution. **Figure 24** shows the QE curves for three nc-Si:H solar cells on Ag/ZnO BR. The QE increases for samples from 0.5 to 1.3 μm, corresponding to an increase of J_{sc}. However, increasing the thickness further to 1.9 μm results

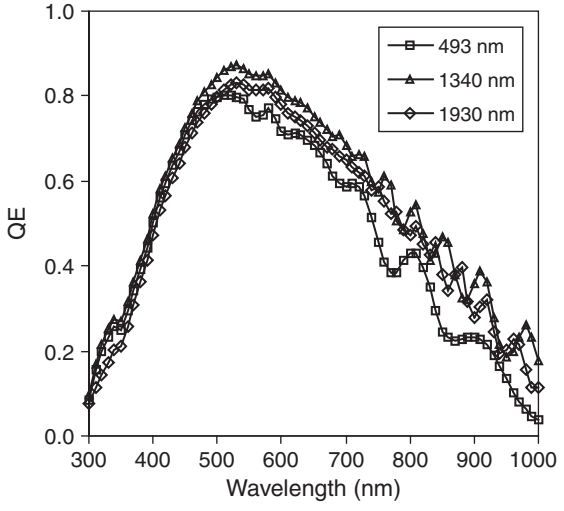

Figure 24 QE of nc-Si:H single-junction solar cells deposited on Ag/ZnO BR with different thicknesses. From Yan B, Yue G, Yang J, *et al*. (2004d) Microstructure evolution with thickness and hydrogen dilution profile in microcrystalline silicon solar cells. *Materials Research Society Symposium Proceedings* 808: 575–580.

in a decrease of QE as well as in V_{oc} and FF (Yan *et al.* 2004c, 2004d). Two mechanisms could be responsible for this phenomenon: the nanocrystallite collision and the increase of nanocrystalline volume fraction. It has been shown that nanocrystallites have a tendency to grow perpendicularly to the growing surface (Nasuno *et al.*, 2000). On a textured surface, nanocrystallites are perpendicular to the local surface and collide with each other when the film grows beyond a certain thickness. The collision of nanocrystallites could cause high-defect densities in the grain boundaries and consequently poorer cell performance. Another mechanism is the increase of nanocrystalline volume fraction and the grain size. As pointed out by Finger *et al.* (2002), large grain sizes could cause microvoids and microcracks, which allow impurities to diffuse into the material. The authors did systematic structural measurements with XRD, Raman, and AFM and confirmed that the increase of grain size and nanocrystalline volume fraction along the deposition direction is the major issue for nc-Si:H solar cells deposited with a constant hydrogen dilution ratio.

To overcome the negative effect of the nanocrystalline evolution on solar cell performance, a hydrogen dilution profiling technique was designed to control the growth of the nanocrystalline phase. A very high hydrogen dilution was used to deposit a seed layer to reduce the thickness of the incubation layer, and then the hydrogen dilution ratio was decreased over time to keep the material close to the transition from the nanocrystalline to the amorphous phases. By optimizing the profiling parameters such as the amount and the rate of change in hydrogen dilution ratio, the nc-Si:H solar cell performance was significantly improved. **Table 7** lists the J–V characteristics of the nc-Si:H solar cells made with various hydrogen dilution profiles. Three baseline cells show a J_{sc} about 22–23 mA cm^{-2}. However, the two cells with 20% longer intrinsic layer deposition time show a lower J_{sc}, mainly due to the reduction in the long wavelength response, as shown in **Figure 25**. By hydrogen dilution profiling, the long wavelength response improved significantly. The cells with the constant hydrogen dilution have an average efficiency of about 6.6%. By using hydrogen dilution profiling, efficiency increases to 8.37%. Recently, Yan *et al.* (2008) used the hydrogen dilution profiling techniques in the modified VHF (MVHF) high-rate-deposited nc-Si:H solar cells and improved the cell efficiency further. An initial active-area

Table 7 *J–V* characteristics of nc-Si:H single-junction solar cells with various hydrogen dilution profiles[a]

			FF				
Sample no.	J_{sc} *(mA cm^{-2})*	V_{oc} *(V)*	*AM1.5*	*Blue*	*Red*	*Eff (%)*	*Comments*
14554	22.58	0.495	0.603	0.652	0.615	6.74	Flat baseline
14568	22.15	0.488	0.599	0.648	0.599	6.48	
14596	22.05	0.482	0.622	0.656	0.605	6.61	
14559	21.48	0.482	0.632	0.678	0.637	6.54	20% thicker than baseline
14562	21.57	0.484	0.652	0.692	0.651	6.81	
14578	23.22	0.482	0.594	0.646	0.631	6.63	Profiling 1
14580	22.58	0.484	0.644	0.688	0.662	7.04	Profiling 2
14612	24.41	0.485	0.616	0.659	0.647	7.29	Profiling 3
14619	24.63	0.492	0.645	0.683	0.641	7.81	Profiling 4
14642	23.42	0.502	0.681	0.706	0.700	8.01	Profiling 5
14660	25.15	0.502	0.663	0.679	0.693	8.37	Profiling 6
14648	22.84	0.521	0.611	0.698	0.627	7.27	Flat

[a] Profiling 1–6 shows progressive improved dilution profile.

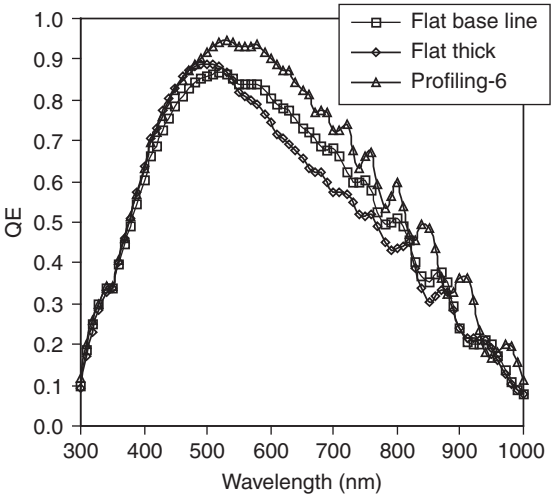

Figure 25 QE curves of the nc-Si:H solar cells made with various hydrogen dilution profiles. From Yan B, Yue G, Yang J, *et al*. (2004d) Microstructure evolution with thickness and hydrogen dilution profile in microcrystalline silicon solar cells. *Materials Research Society Symposium Proceedings* 808: 575–580.

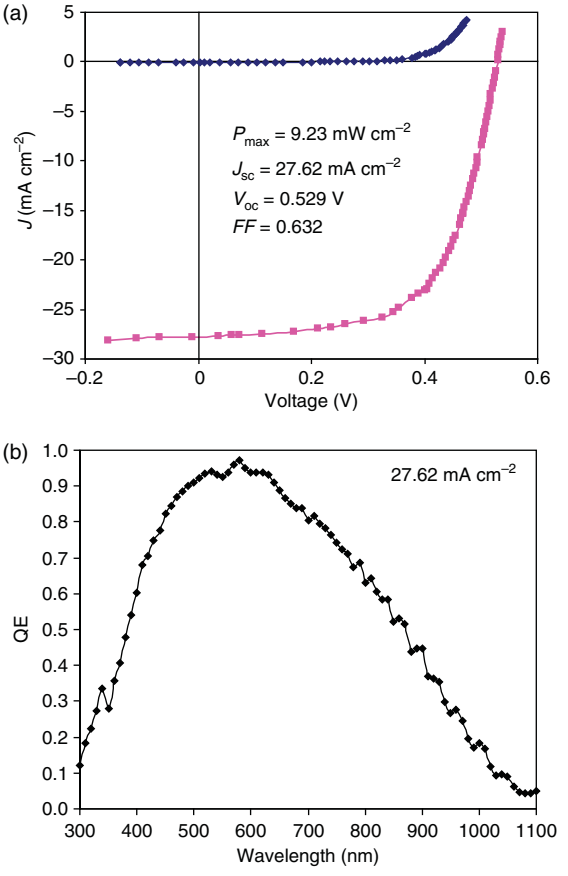

Figure 26 *J–V* characteristics (a) and quantum efficiency (b) of a nc-Si:H solar cell with an active area of 0.25 cm^2 in its initial state. From Yan B,Yue G, Yan Y, et al. (2008b) Correlation of hydrogen dilution profiling to material structure and device performance of hydrogenated nanocrystalline silicon solar cells. *Materials Research Society Symposium Proceedings* 1066: 61–66.

efficiency of 9.2% has been achieved. **Figure 26** shows the *J–V* characteristics and QE curve of the high performance nc-Si:H solar cell. **Figure 27** shows the cross-sectional TEM image of an nc-Si:H solar cell made with a hydrogen dilution profiling that resulted in high cell performance (Yan *et al*., 2008b). The detailed analysis showed that the nanocrystalline volume fraction was essentially uniform with a slight decrease with the thickness. Yue *et al*. (2006) showed that the slightly inversed nanocrystalline

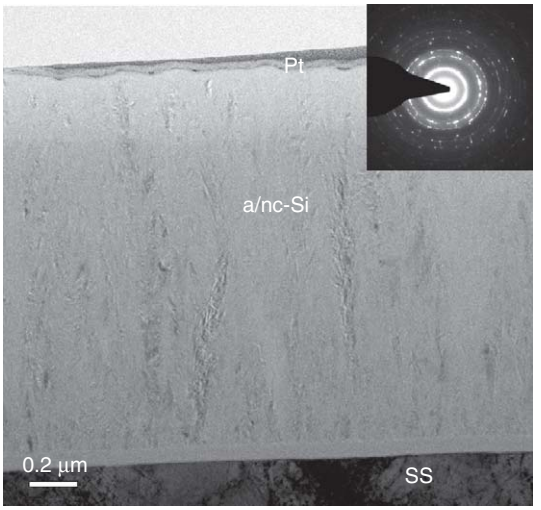

Figure 27 Cross-sectional TEM image of an nc-Si:H solar cell made with hydrogen dilution profile. From Yan B, Yue G, Yan Y, *et al*. (2008b) Correlation of hydrogen dilution profiling to material structure and device performance of hydrogenated nanocrystalline silicon solar cells. *Materials Research Society Symposium Proceedings* 1066: 61–66.

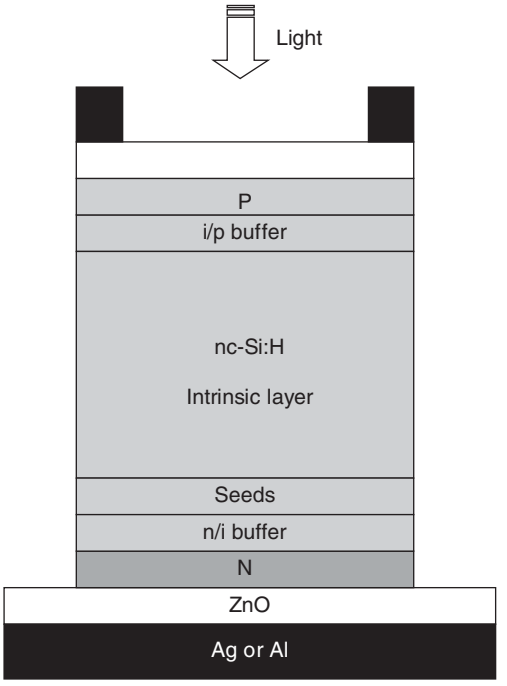

Figure 28 Schematic drawing of a high-efficiency nc-Si:H solar cell on a Ag/ZnO back reflector-coated stainless steel substrate.

evolution was beneficial for nc-Si:H solar cell performance. The inversed nanocrystalline evolution is especially important for the n–i–p structures, where the top ITO is not an impurity barrier, thus a more compact material structure in the top region effectively reduces the possibility of impurity diffusion into the intrinsic layer.

Recently, the hydrogen dilution profiling technique has been widely used by many laboratories and has been accepted as an effective method to improve nc-Si:H cell performance (Gordijn *et al*., 2005, 2006; Das *et al*., 2006).

4. *nc-Si:H solar cell design.* Generally speaking, highly efficient solar cells not only need high-quality materials in all the layers, but also an optimized device design. In the case of nc-Si:H solar cells, the device design is more complicated than that of a-Si:H because of the different band gaps in the doped layers and the intrinsic layer. **Figure 28** shows the schematics of an nc-Si:H cell structure on an Ag/ZnO-coated stainless steel substrate. The n-layer can be either n-type a-Si:H or nc-Si:H. The n/i buffer is normally a thin layer of a-Si:H, which has two functions: reduce the possibility of phosphorus diffusion and provide a potential barrier preventing photo-generated holes from diffusing back to the n-layer. The seeding layer is used to reduce or eliminate the a-Si:H incubation layer, thus providing a well-controlled interface for nc-Si:H to grow. The i/p buffer layer is also a thin a-Si:H layer, which not only has similar functions as the n/i buffer layer but also provides an extra capping layer for protecting the nc-Si:H intrinsic layer by blocking the shunt current channels through microfilaments.

Dark current versus voltage (J–V) measurements and their correlations to cell performance showed that a proper i/p buffer layer reduced the dark current significantly and made the dark J–V characteristics follow the standard diode characteristics (Yue *et al*., 2008). As a result, the V_{oc} of nc-Si:H solar cells was improved. However, if the i/p buffer layer was too thick, extra series resistance caused a reduction in FF.

6.08.5.2.4 Current matching in multijunction solar cells

For multijunction solar cells, the individual component cells are connected in series through the tunnel junctions. Generally speaking, the V_{oc} of a multijunction solar cell is close to the sum of V_{oc} of all the component cells under respective illumination conditions in the multijunction structure. However, the J_{sc} is close to the smallest J_{sc} of all the component

cells. In principle, if the component cells all have good material qualities, a matched current between the component cells would result in high solar cell efficiency. However, the component cells usually have different material qualities. In this case, a proper current mismatch with the limiting cell having a better material quality than the other component cells should give a better efficiency (Guha and Yang, 1992). Because optimized a-Si:H films have better material properties such as lower defect density and higher carrier mobility than optimized a-SiGe:H, a top cell limited current mismatch is desirable for conventional a-Si:H/a-SiGe:H/a-SiGe:H triple-junction solar cells. Furthermore, a-SiGe:H cells normally show more LID than a-Si:H cells and a large current mismatch is needed if one seeks high stable solar cell efficiency.

For multijunction solar cells with nc-Si:H bottom cell, a bottom cell limited-current mismatch results in a better cell efficiency because the nc-Si:H material has a better quality than a-Si:H and a-SiGe:H. In addition, nc-Si:H cells show very little LID, a bottom cell limited-current mismatch leads to a high stable efficiency. Several multijunction structures with nc-Si:H intrinsic layers have been investigated, including a-Si:H/nc-Si:H double-junction, a-Si:H/a-Si:H/nc-Si:H triple-junction, a-Si:H/a-SiGe:H/nc-Si:H triple-junction, and a-Si:H/nc-Si:H/nc-Si:H triple-junction structures. Considering cell efficiency and the simplicity of manufacturing, the a-Si:H/nc-Si:H double-junction structure is attractive for most manufacturers. However, there is a problem about current mismatch. For an nc-Si:H single-junction cell, a J_{sc} of 26–31 mA cm^{-2} can be obtained with optimized nc-Si:H materials and light trapping. For an a-Si:H top cell, it needs a very thick intrinsic layer to generate enough current, 13–15 mA cm^{-1}, to match the current from the nc-Si:H bottom cell in an a-Si:H/nc-Si:H double-junction structure. With a thick intrinsic layer, the a-Si:H top cell suffers from LID. In order to resolve this issue, an inter-reflection layer was introduced by the Neuchatel group (Fischer *et al.*, 1996) and subsequently used by Kaneka Co. (Yamamoto *et al.*, 2003; Fukuda *et al.*, 2006). The a-Si:H/nc-Si:H double-junction cell structure with an inter-reflection layer is displayed in **Figure 29**, where a dielectric material with an optical index around 2.0 is inserted between the a-Si:H top and the nc-Si:H bottom cells. A portion of the incident light is reflected back into the a-Si:H top cell due to the different optical indices between the inter-reflection layer and the silicon layer. For

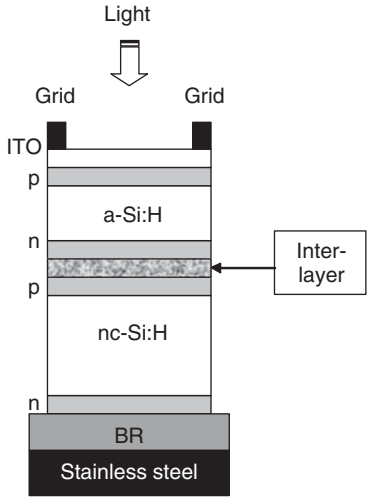

Figure 29 An a-Si:H/nc-Si:H double-junction structure with a transparent interreflection layer.

a-Si:H or nc-Si:H, the average optical index is about 3.6. If an interlayer has an optical index of 2.0, the first reflection from the interlayer is about 8%; while for an optical index of 1.7, the reflection is about 13%. The reflected light is absorbed by the a-Si:H top cell and increases the top cell current; at the same time, the bottom cell current is reduced (Fischer *et al.*, 1996). Enhancement of the top cell current and the reduction of the bottom cell current depend not only on the optical index but also on the thickness of the interlayer. Therefore, one can optimize the current mismatch by choosing a proper dielectric material of appropriate optical index and conductivity and by optimizing the interlayer thickness. The commonly used dielectric materials are ZnO and SnO_2, which are used in TCO for glass substrates or BRs on stainless steel or polyimide. In order to reduce the interlayer optical index, the Neuchatel group has used doped SiO_x as an interlayer. With P doping, the SiO_x layer can have conductivity high enough for the current flow without significant electrical losses.

Because the light reflected by the interlayer may not be totally absorbed by the top cell, especially the long wavelength portion, the gain in the top cell current is equal to or less than the loss in the bottom cell current in most cases. In addition, the interlayer may have some absorption. Therefore, one should not expect to have extra gain in the total current (top cell current + bottom cell current). Recently, Kaneka Co. reported an optimized interlayer with an optical index of 1.7 (Fukuda *et al.*, 2006).

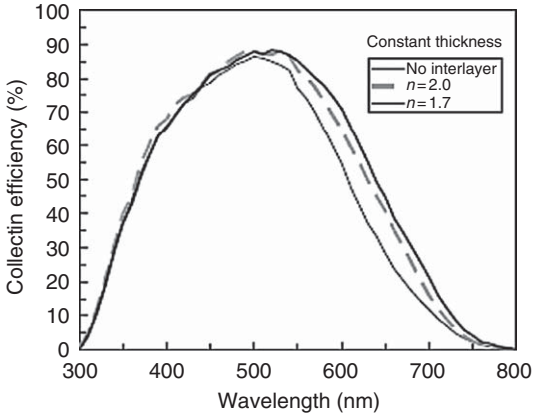

Figure 30 Collection efficiency curves of a-Si:H top cell with two kinds of interlayer ($n = 2.0$ and 1.7) with the same thickness and without interlayer. The thickness of each layer (a-Si:H top, interlayer, nc-Si bottom) is the same for all examples. The curve with low responses in the long wavelength region is with no interlayer, the middle one has an interlayer of $n = 2.0$, and the one with high long-wavelength responses has an interlayer of $n = 1.7$. From Fukuda S, Yamamoto K, Nakajima A, *et al*. (2006). High-efficiency thin film silicon hybrid cell and module with newly developed interlayer. In: Poortmans J, Ossenbrink H, Dunlop E, and Helm P (eds.) *Proceedings of the 21st European Photovoltaic Solar Energy Conference*, pp. 1535–1538. Munich, Germany: WIP Renewable Energies.

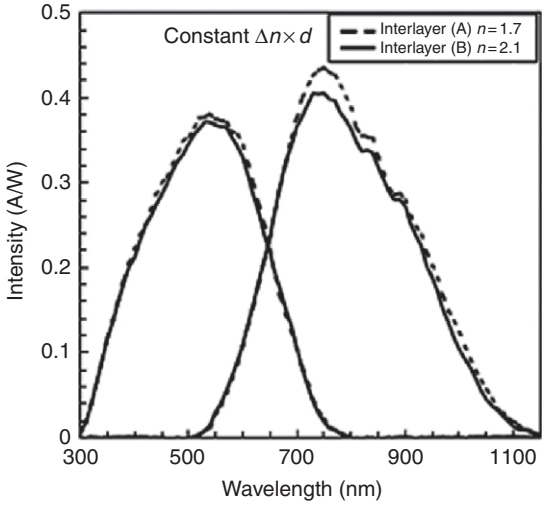

Figure 31 The spectral response comparison of two a-Si:H/interlayer/nc-Si:H solar cells with different kinds of refractive index for constant $\Delta n \times d$ product, where Δn is difference in the index of refraction between the interlayer and the surrounding silicon layers ($n = 3.6$), and d is the thickness of the interlayer, respectively. Note that the higher spectral response in the bottom cell is obtained for interlayer with lower refractive index (A) while keeping the $\Delta n \times d$ product. From Fukuda S, Yamamoto K, Nakajima A, *et al*. (2006) High-efficiency thin film silicon hybrid cell and module with newly developed interlayer. In: Poortmans J, Ossenbrink H, Dunlop E, and Helm P (eds.) *Proceedings of the 21st European Photovoltaic Solar Energy Conference*, pp. 1535–1538. Munich, Germany: WIP Renewable Energies.

Figure 30 shows the a-Si:H top cell QE curves in a-Si:H/nc-Si:H double-junction cells without an interlayer and with different interlayers with optical index of 2.0 and 1.7. It clearly showed that the interlayer with an optical index of 1.7 enhances the top cell current more than the one with an optical index of 2.0. They also compared the bottom cell current and found that with an optical index of 1.7, as shown in **Figure 31**, the nc-Si:H bottom cell current was also higher than the one with an optical index of 2.1. With the improved cell structure, they achieved a cell efficiency of 15.0%, and module efficiency of 13.4% with an area of 3827 cm^2.

6.08.5.2.5 Tunnel junction

A multijunction cell incorporates one or more internal tunnel junctions at the interface of the n- and p-layers of the adjacent component cells. Any parasitic junction loss at the tunnel junction, electrical or optical, leads to a deleterious effect on the overall characteristics of the device (Hou *et al*., 1991). The property of the doped layers can have a significant effect on the tunnel junction and thereby may affect the multijunction device performance.

A technique was developed by Banerjee *et al.* (1994a) to characterize the internal tunnel junction of a multijunction cell. The device structure used for this purpose, referred to as the nipn structure, consists of the bottom n_1 i_1 p_1 cell followed by the n_2 layer. The nipn device is coated with ITO dots for measurement. The *I–V* characteristics of the nipn structure have been found to be sensitively dependent on the quality of the p_1/n_2 tunnel junction. Evaluation of the nipn device, therefore, provides a useful way to investigate the quality of the internal junctions in a multijunction cell.

Since the microcrystalline n-layer is more transparent and conductive than its amorphous counterpart, attempts were made by Yang *et al.* (1997, 2003) to use this material to obtain improved tunnel-junction characteristics. A pair of a-Si:H/a-Si:H double-junction cells was made under substantially the same deposition conditions. The only difference between the two devices is that one uses an amorphous n-layer, while the other uses a

microcrystalline n-layer in the tunnel junction. Even though the use of microcrystalline n-layer allows more light to go to the bottom cell, it was found that the V_{oc} value for the tandem cell having a microcrystalline n-layer is much lower than the corresponding cell with an amorphous n-layer in the tunnel junction. The lowering of V_{oc} may be due to band-edge discontinuity between the amorphous i and microcrystalline n or the intermixing of dopants in thin microcrystalline layers, or both.

Yang *et al.* (1997) have developed a thin buffer layer that can be inserted between the microcrystalline p- and n-layers and also between the microcrystalline n-layer and the adjacent amorphous i-layer to alleviate the problem. Incorporation of the new tunnel-junction structure gives rise to improved cell characteristics, as evidenced by the higher total current and lower series resistance. Incorporation of such tunnel junction in the triple-cell structure has resulted in high solar cell efficiency.

6.08.5.2.6 Top conducting oxide

The top conducting oxide in the substrate-type configuration is usually ITO. Both reactive evaporation and sputtering have been used successfully. A quarter-wavelength thickness is used to serve the purpose of antireflection coating. Typical sheet resistivity is 50–100 Ω/square, and additional grid lines are deposited onto the ITO to reduce series resistance losses. In order to reduce optical losses, the ITO layer needs to be very transparent. Typical loss associated with the state-of-the-art ITO lowers $\mathcal{J}_{sc}$ by about 0.5 mA cm^{-2} (Hoffman and Glatfelter, 1993).

For the superstrate-type structure, the light enters through the conducting oxide that is directly deposited on the glass. Both tin oxide and zinc oxide have been used. The conducting oxide is usually thick, 500–1000 nm, to obtain the necessary texture, and this leads to lowering of $\mathcal{J}_{sc}$ by 1–2 mA cm^{-2}.

6.08.5.3 High-Efficiency Solar Cell and Module

Over the past 30 years, many groups in the industries, universities, and other research institutions have worked on the research and development of a-Si:H, a-SiGe:H, and nc-Si:H solar cells in the areas from fundamental material properties to large-area solar module fabrications. The solar cell efficiency has been steadily improving. **Table 8** lists the United Solar's initial and stable efficiencies achieved with different cell structures, where no nc-Si:H was used (Yang *et al.*, 1997, 2003). The highest initial and stable active-area efficiencies were achieved using an a-Si:H/a-SiGe:H/a-SiGe:H triple-junction structure. It is interesting to note that as one moves from the a-Si:H single-junction to the a-Si:H/a-Si:H double-junction structure, the stabilized efficiency increases from 9.3% to 10.1%. Incorporation of Ge in the bottom cell increases the efficiency further to 12.4%. Using a triple-junction, triple-band gap structure results in the highest stable efficiency of 13%. We should point out that unless there is a fundamental solution to LID, the triple-junction structure is the only option for amorphous silicon- and silicon-germanium-alloy-based technology by which further improvement in efficiency can be made.

In the past 10 years, the efficiency of multijunction cells incorporating a-Si:H and a-SiGe:H has not shown any improvement. Since the development of nc-Si:H solar cell by the Neuchatel group (Meier *et al.*, 1994), multijunction solar cell efficiency has been improving and has now surpassed

Table 8 Highest stable cell efficiencies (active area ~0.25 cm^2) and their initial values at United Solar for different junction configurations

Structure	*State*	J_{sc} (mA cm^{-2})	V_{oc} (V)	*FF*	η (%)
a-Si:H	Initial	14.65	0.992	0.730	10.6
single junction	Stable	14.36	0.965	0.672	9.3
a-Si:H/a-Si:H same-gap	Initial	7.9	1.89	0.76	11.4
double junction	Stable	7.9	1.83	0.70	10.1
a-Si:H/a-SiGe:H dual-gap	Initial	11.04	1.762	0.738	14.4
double junction	Stable	10.68	1.713	0.676	12.4
a-Si:H/a-SiGe:Ha-SiGe:H	Initial	8.57	2.357	0.723	14.6
triple junction	Stable	8.27	2.294	0.684	13.0

Table 9 The highest initial solar cell efficiencies achieved with nc-Si:H in different cell structures

Structure	*Institute*	*Area (cm^2)*	*Initial efficiency (%)*	*References*
nc-Si:H single junction	Jülich	1.0	10.3	Mai *et al.* (2005)
a-Si:H/nc-Si:H double junction	Kaneka	1.0	14.7	Yamamoto *et al.* (2002)
a-Si:H/a-Si:H/nc-Si:H triple-junction	Kaneka	1.0	15.0	Fukuda *et al.* (2006)
a-Si:H/a-SiGe:H/nc-Si:H triple junction	United Solar	0.25	15.4	Yan *et al.* (2008)
a-Si:H/nc-Si:H/nc-Si:H triple junction	United Solar	0.25	14.1	Yue *et al.* (2006)

the record efficiency achieved with the conventional a-Si:H and a-SiGe:H multijunction structures (Yang *et al.*, 1997, 2003). **Table 9** shows a summary of the highest initial solar cell efficiencies achieved with different cell structures. One can see that with nc-Si:H in the bottom cell, and in some structures in the middle cell, the multijunction cell efficiency has improved significantly. The highest initial active-area cell efficiency is 15.4% achieved by United Solar, with the J–V characteristics and QE shown in **Figure 32**. The progress in the improvement of solar cell efficiency with nc-Si:H bottom cells in triple-junction structures made in United Solar is shown in **Figure 33**.

In order to ensure that any new solar cell structure is suitable for mass production, the small-area cell results must be translated to large areas. **Tables 10** and **11** summarize the module efficiencies achieved with amorphous materials and amorphous/nanocrystalline materials in the multijunction cell structures. Because of the low LID in the nc-Si:H-based modules (3–10%), most groups only reported the initial efficiencies. It is observed that use of nc-Si:H in the bottom cell intrinsic layer results in an increase of module efficiency as well. Currently, many companies are focusing on the development of large-area, high-rate nc-Si:H deposition technologies for mass production. In the very near future, high-efficiency thin-film solar panels with nc-Si:H-based multijunction cells will be in the market. The target stable module efficiencies will be in the range of 8–12%.

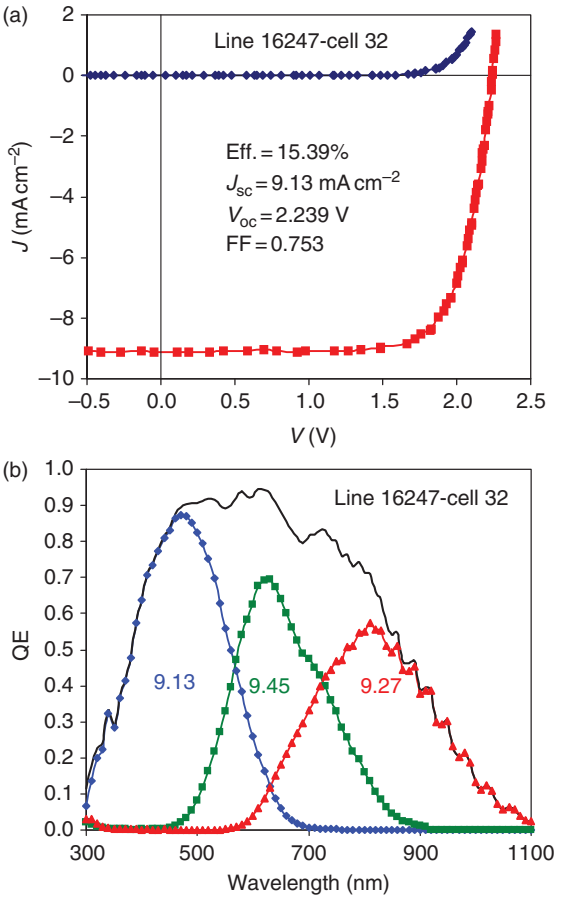

Figure 32 (a) J–V characteristics and (b) quantum efficiency curves of an a-Si:H/a-SiGe:H/nc-Si:H triple-junction cell with an initial active-area efficiency of 15.4%. From Yan B, Yue G, Yang J, and Guha S (2008c) Correlation of current mismatch and fill factor in amorphous and nanocrystalline silicon based high efficiency multi-junction solar cells. In: *Proceedings of the 33rd IEEE Photovoltaic Specialists Conference*, Paper No. 257 (CD). New York: IEEE.

6.08.6 Manufacturing Technology

The first application of a-Si:H alloy solar cells was for calculators, and even today these cells are being used to power a variety of consumer applications that require small amount of power. Today, a-Si:H alloy solar panels are used for a wide range of applications from battery charging to large-scale grid-connected applications. Two different approaches have been adopted for production of superstrate- and substrate-type solar cell structures. Detailed discussions are given below.

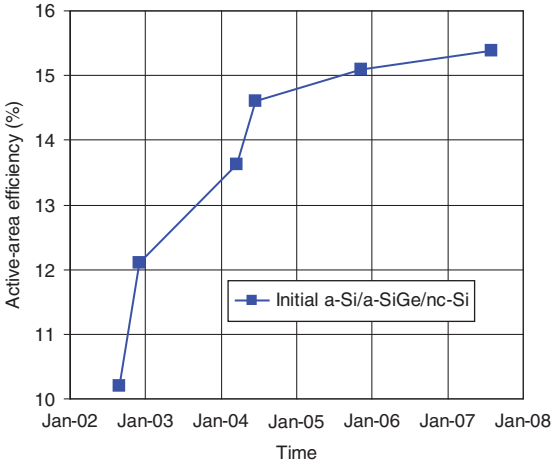

Figure 33 Progress of initial active-area cell efficiency with nc-Si:H in the bottom cell of triple-junction structures made by United Solar.

Most of the manufacturers use monolithic interconnection of the cells using a superstrate structure. A typical flowchart of a manufacturing line for making superstrate-type solar modules is shown in **Figure 34**. Window glass plates are first washed; a thin (~50 nm) layer of silicon dioxide is deposited onto the glass, followed by about 600–1000 nm of tin oxide. The tin oxide is then laser scribed to form the front contacts of the individual cell segments. The glass plate is next loaded into the deposition systems where the different layers of the a-Si:H alloys are deposited, followed by the deposition of ZnO. Another laser scribing is done, followed by deposition of Al or Ag. Another laser scribing completes the series-interconnect steps. **Figure 35** illustrates a series-interconnected superstrate-type solar module. Final encapsulation is done by bonding another glass plate to the cell structure. Several manufacturers have come out with glass-in/panel-out concept, where all the processes are done in an automated process, thus reducing the labor cost. Sizes from 1000 cm^2 to about 6 m^2 are being used (Lechner *et al.*, 2008) and several equipment manufacturers (Kadam *et al.*, 2008; Meier *et al.*, 2008) are offering turnkey systems or custom-built equipment to PV manufacturers.

The biggest challenge is uniformity over large area. Since many individual cell strips are series interconnected, the cell with the lowest current (smallest thickness) will limit the module performance. While there has been a great deal of progress in achieving uniformity over large area for a-Si:H deposition, nc-Si:H poses different challenges. Many manufacturers are using vhf deposition reactors to increase the deposition rate. Use of vhf demands special cathode design so that the field distribution is uniform, and innovative antenna array design (Takagi *et al.*, 2006) and multi-ladder power input structures (Mashima *et al.*, 2006) have been proposed.

Instead of using glass or stainless steel, polymeric substrates have also been used by several groups, including PowerFilm Inc., Flexcell, and United Solar Ovonic. United Solar uses polyimide bonded to stainless steel to carry out the roll-to-roll operation. The processing for cell making is the same as used in their production line. The stainless steel is

Table 10 Initial and stable module efficiencies achieved with a-Si:H and a-SiGe:H materials in multijunction structures

Structure	*Institute*	*Area (cm^2)*	*Initial Eff. (%)*	*Stable Eff. (%)*	*Reference*
a-Si:H/a-SiGe:H/a-SiGe:H triple junction	United Solar	920	11.5	10.5	Banerjee *et al.* (1999)
a-Si:H/a-SiGe:H double junction	Sanyo	8252	11.2	10.0	Okamoto *et al.* (2001)
a-Si:H/a-SiGe:H double junction	BP Solar	842	10.5	9.1	Arya *et al.* (1994)
a-Si:H/a-SiGe:H double junction	Fuji Electric	3200	10.1	9.0	Yoshida *et al.* (2000)

Table 11 Initial module efficiencies achieved with a-Si:H and nc-Si:H materials in multijunction structures

Structure	*Institute*	*Area (cm^2)*	*Initial Eff. (%)*	*Reference*
a-Si:H/nc-Si:H/nc-Si:H triple junction	Canon	801.6	13.2	Saito *et al.* (2005)
a-Si:H/nc-Si:H double junction	Kaneka	3827	13.4	Yamamoto *et al.* (2006)
a-Si:H/nc-Si:H double junction	MHI	2394	12.9	Takatsuka *et al.* (2006)
a-Si:H/nc-Si:H double junction	IPV Julich	676	10.1	Rech *et al.* (2003)
a-Si:H/nc-Si:H double junction	United Solar	460	10.6	Yan *et al.* (2004)

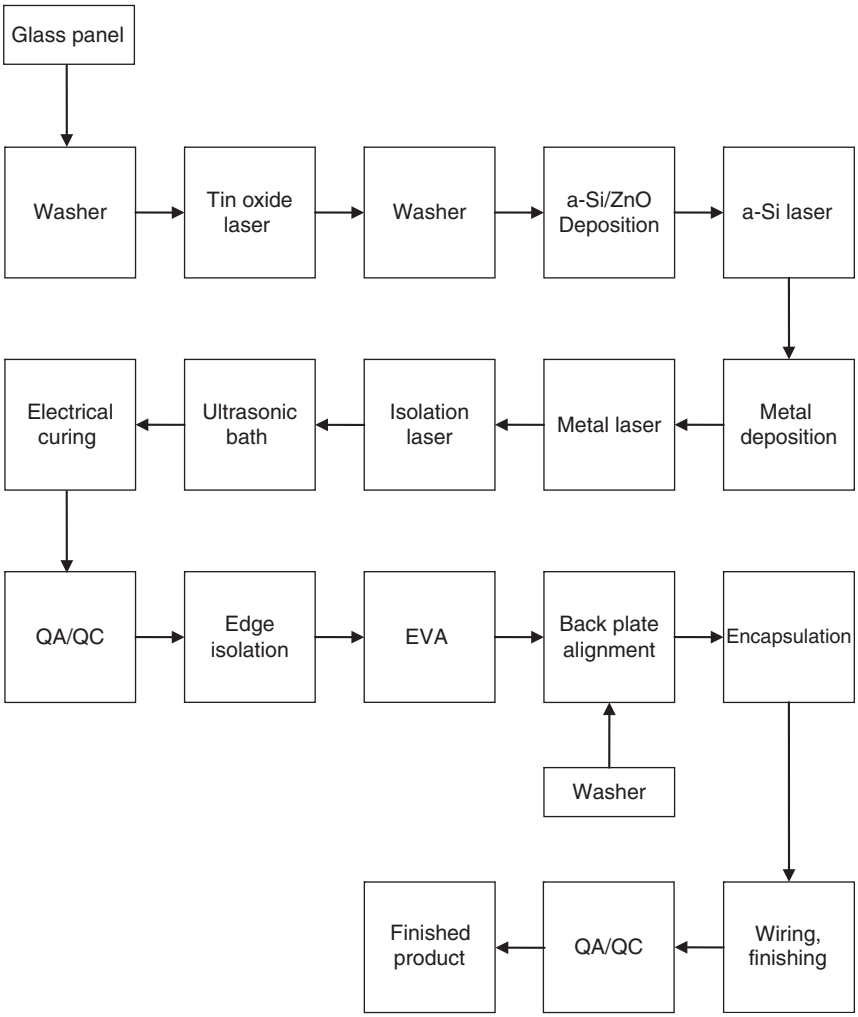

Figure 34 A typical flowchart of a manufacturing line for making superstrate-type solar modules.

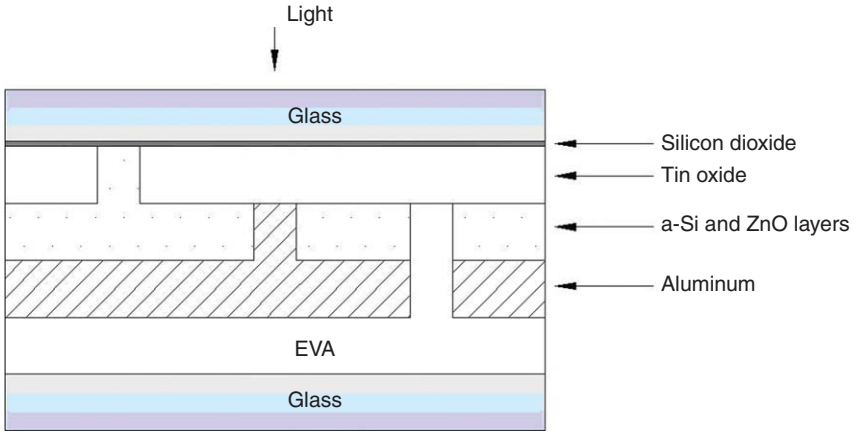

Figure 35 A series-interconnected superstrate-type solar module.

removed after the cell is completed, and the cells are interconnected to make lightweight laminates. Since the substrate is insulating, monolithic modules can also be made. A step-and-roll process has been developed (Takano *et al.*, 2006), in which using a combination of roll-to-roll processing and laser drilling series-interconnected laminates can be fabricated. The outline of the process is as followed:

1. Series connection holes are punched on the polymer substrate.
2. Metal electrodes are sputtered on both sides of the substrates.
3. Current collection holes are made by punching.
4. The different layers of the cell are deposited on the polymer.
5. Layers deposited on both sides of the substrate are divided into unit cells by laser patterning.
6. The interconnected cells are laminated using ethylene tetrafluoroethylene (ETFE) and ethylene vinyl acetate (EVA).

Another approach to take advantage of roll-to-roll application together with monolithic integration has been developed where tin oxide, active layers for the cell, and the BR are deposited sequentially on a roll of Al substrate (Hamers *et al.*, 2008). After the cell processing and encapsulation, the Al substrate is etched off.

A roll-to-roll manufacturing process has been developed (Izu and Ellison, 2003) for the production of solar panels using the substrate-type structure. Stainless steel rolls, typically 1.5-miles long, 14-inches wide, and 0.005-inch thick, go sequentially through four machines that serve the purpose of (1) washing, (2) depositing the BR layers, (3) depositing the a-Si:H and a-SiGe:H layers, and (4) depositing ITO, which serves as an antireflection coating. The coated web is next processed to make a variety of lightweight, flexible, and rugged products. The processing steps involve (1) cutting of the web into slabs, (2) short and shunt passivation and etching of ITO to define strip-cell area, (3) attaching electrodes and grids, and (4) final assembly involving interconnection of the strips and lamination.

A brief description of the various operations is given below.

Wash machine. The roll of stainless is washed in a roll-to-roll processing system, which transports the web through a detergent cleaning station, multiple deionized water rinsing baths, and an infrared drying oven. The clean, dry, and dust-free web is next loaded into the BR machine. One roll is processed at a time that runs through the machine at a speed of 15 ft min^{-1}.

BR machine. The BR machine sequentially deposits a reflective metal (Al) layer and a metal oxide buffer layer (ZnO) onto the cleaned stainless steel web by magnetron sputtering. Reactive sputtering is used for the ZnO layer deposition. The BR layers provide the ohmic contact between the stainless steel and the a-Si:H alloy. The layers are deposited at a high temperature to obtain a textured surface so as to facilitate multiple reflections. Three rolls are processed at a time running through the machine at about 7 ft min^{-1}.

Amorphous silicon alloy deposition machine. The web coated with the BR is next loaded into the a-Si:H processor (**Figure 36**), which is about 300 ft long and has, in addition to the pay-off and take-up

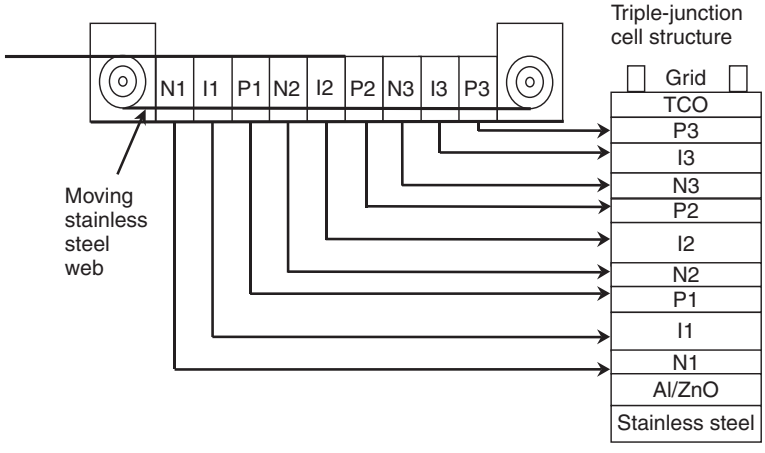

Figure 36 Schematic diagram of a roll-to-roll a-Si:H triple-junction solar cell processor. From Yang J, Banerjee A, and Guha S (2003) Amorphous silicon based photovoltaics – from earth to the ''final frontier''. *Solar Energy Materials and Solar Cells* 78: 597–612.

chambers, multiple chambers to deposit the nine layers of the triple-cell structure. The deposition chambers have multiple cathodes to ensure power uniformity. The adjacent chambers for the intrinsic and doped layer deposition are separated by proprietary gas gates to eliminate contamination of the dopant gases in the intrinsic layers. The individual layers are grown by plasma-enhanced chemical vapor deposition process at a pressure of about 1 Torr, and all the layers are deposited simultaneously and consecutively on the moving web (**Figure 36**) to complete the triple-junction cell structure. Special cathode designs ensure improved gas utilization and uniformity of the deposited layers. The gas manifolds for introducing silane and germane for the a-SiGe:H alloy component cells are specially designed to facilitate band gap profiling (Guha *et al.*, 1989). The process conditions used for the deposition of the p-type layer facilitate microcrystalline growth (Izu and Ellison, 2003).

Six rolls move through the machine at a speed of about 2.2 ft min^{-1}, three on each side of the cathode placed in between, and the rolls are on the same vertical plane. The machines are provided with diagnostic tools to determine layer thickness and cell parameters such as open-circuit voltage.

Indium tin oxide deposition machine. The final step in the deposition process is reactive magnetron sputtering of ITO, which serves as the antireflection coating and also provides the top conducting contact. Typical deposition temperature is 200 °C. Three rolls are processed at a time running at about 7 ft min^{-1}. **Figure 37** illustrates the four roll-to-roll processes.

Module assembly operation. The module assembly operation is semi-automated to facilitate flexibility in the choice of the product line while ensuring low cost and reliability. The finished roll of the coated web is first cut into 9.4 inch × 14 inch slabs. The slabs are then processed to define cell size, passivated to remove shunts and shorts (Guha *et al.*, 1998), and tested to ascertain quality. Grid wires and contact pads are next applied, and the cells are then interconnected and the cellblock laminated to provide protection against outside atmosphere. The finished modules undergo performance measurement under global AM1.5 illumination and a high pot (hi-pot) test before they are shipped out. The cell assembly steps are shown in **Figure 38**.

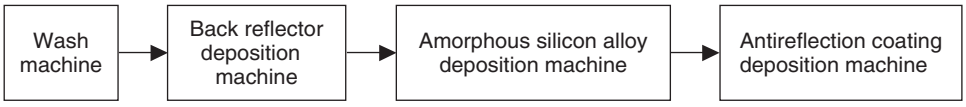

Figure 37 Schematic diagram of the four roll-to-roll processes.

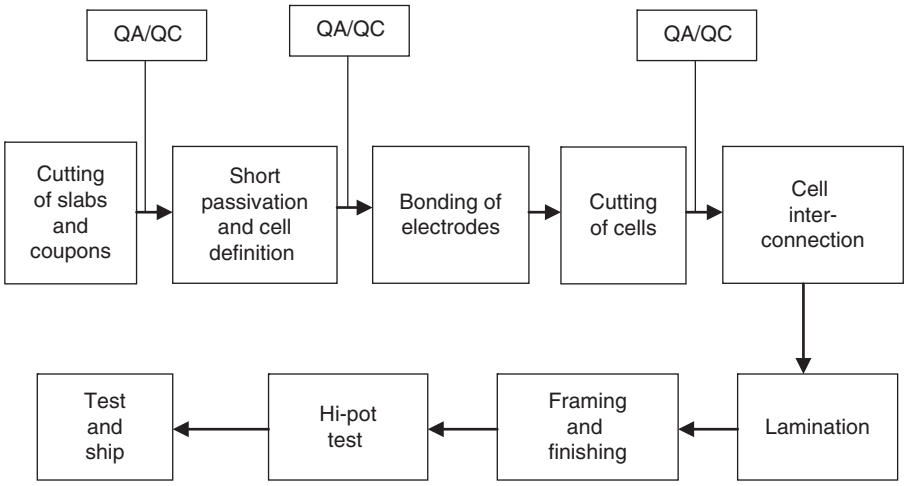

Figure 38 Block diagram of the module fabrication process. From Yang J, Banerjee A, and Guha S (2003) Amorphous silicon based photovoltaics – from earth to the ''final frontier''. *Solar Energy Materials and Solar Cells* 78: 597–612.

6.08.7 Product Advantage and Market

6.08.7.1 Product Advantage

Major motivation to use a-Si:H in PV products came from the following:

- Since only a thin film (<1 μm) is needed as opposed to several hundred micrometers for crystalline silicon solar cells, the material cost is low.
- The highest temperature in processing is less than 300 °C as opposed to greater than 1000 °C for crystalline silicon. The energy payback time is therefore low.
- Since a-Si:H has a larger band gap than that for silicon crystals, the temperature coefficient for power is lower (–0.2% per °C vs. –0.5% per °C). Products based on a-Si:H therefore produce more electricity per rated power than those with crystalline silicon under real-life condition.
- Multijunction cells operate well under scattered light; the products also work better under low light conditions.
- It is possible to put bypass diodes across each cell when the cells are interconnected in series; the product therefore works better under partial shade.
- Since the material has extensive use in flat-panel displays, there is a technology base for large-area deposition.
- Products can be made on flexible substrates that can be easily integrated with roofs.

6.08.7.2 Independent Verification of Performance

For any new product to obtain a major market share, independent verification of the above features was necessary. A major worry was the phenomenon of LID. Independent verifications for degradation of modules based on different structures have been carried out in many laboratories. **Figure 39** shows the data reported by researchers from ISPRA (Nikolaeva-Dimitrova *et al.*, 2008).

Most manufacturers today rate their products at the stable power output; the degradation in the field should be no more than what is expected from solar panels using any established technology. National Renewable Energy Laboratory (NREL) has been monitoring an *UNI-SOLAR*® array since 1994 (Anderson and Schulic, 2005), and reported less than 1% annual degradation that is no more than what is expected from arrays with conventional technology.

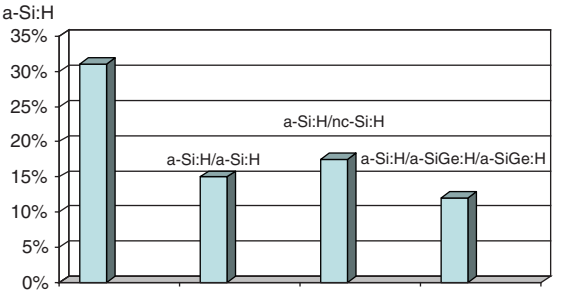

Figure 39 Percentage degradation for various module structures. From Nikolaeva-Dimitrova M, Skoczek A, Kenny RP, and Dunlop ED (2008) Outdoor module performance of single, double and triple-junction silicon based thin film technologies. In: *Proceedings of the 23rd European Photovoltaic Solar Energy Conference*, pp. 2079–2083. Munich, Germany: WIP Renewable Energies.

Some recent installations show even better stability; Florida Solar Energy Center (Pethe *et al.*, 2008) has reported only 0.6% annual degradation over a period of 24 months, as shown in **Figure 40**. There are several other reports (Tawada *et al.*, 2004; Takatsuka *et al.*, 2006, 2006b) showing similar stable behavior.

Many reports have also come out demonstrating the superior kWh/kW performance of a-Si:H-based products over conventional ones (Gregg *et al.*, 2005; van Cleef *et al.*, 2001; Möbius *et al.*, 2008). In **Figure 41**, the performance of a 2-kW array based on a-Si:H modules is compared with that for a polycrystalline silicon-based PV array with the same nameplate rating. The location was Santa Cruz, CA, USA. It is clear that throughout the years, an a-Si:H-based array produces about 20% more electricity than the crystalline silicon counterpart, even though the nameplate ratings are the same.

Similar data for an installation in Hokkaido, Japan (Kaneka report), is shown in **Figure 42**. Again, an a-Si:H-based array is shown to produce 10% more electricity than conventional products for the same power rating.

While a-Si:H PV products are deployed for many different markets, flexible a-Si:H products have some unique advantages for roof-top applications (Guha, 2005). It is interesting to point out that about 64% of PV products installed worldwide are on rooftops. Typically, in order to mount a conventional PV product on the roof, one has to mount a support structure, bolt that down to the roof, and next the panels are fixed to the support structure (**Figure 43**). There are associated hardware and labor costs. The a-Si:H alloy products can be made flexible and lightweight. Some products are provided with an adhesive and a release paper at the back. The products can be

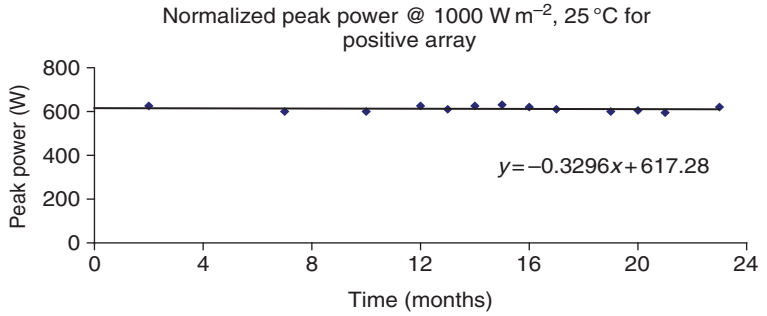

Figure 40 Performance of an a-Si:H PV array. From Pethe SA, Kaul A, and Dhere NG (2008) Statistical data analysis of thin film photovoltaic modules deployed in hot and humid climate of Florida. *Proceedings of the SPIE* 7048: 70480T-1–70480T-8.

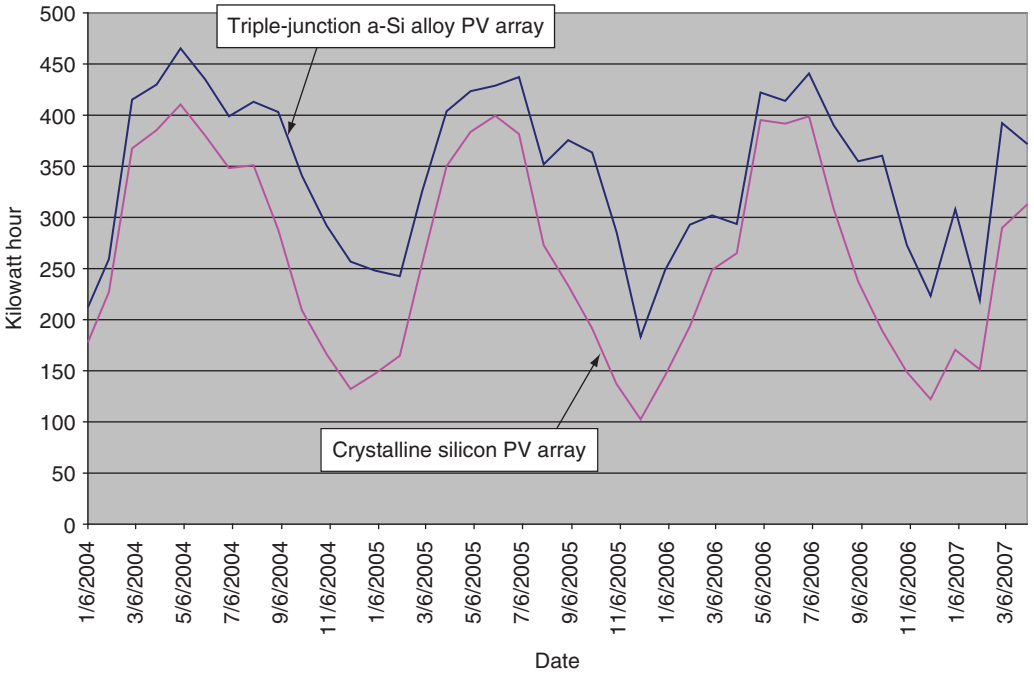

Figure 41 Electricity output from two arrays in Santa Cruz, CA, USA, with the same nameplate rating based on triple-junction a-Si:H modules and crystalline silicon modules.

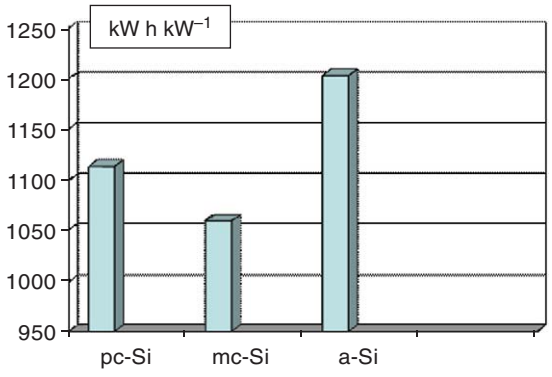

Figure 42 Electricity output per rated power in Hokkaido, Japan, using three different technologies.

rolled and shipped to the site, the release paper removed, and the products can be directly bonded to the roof (**Figure 43**).

These lightweight and flexible building-integrated PV (BIPV) products have been receiving a great deal of attention, and **Figure 44** shows the world's largest roof-top installation of 12 MW in Zaragoza, Spain, using flexible a-Si:H BIPV products.

6.08.7.3 Market

Over the past decade, a handful of manufacturers has been selling a-Si:H products, improving their efficiency and reliability. It is quite common to

Figure 43 Deployment of rigid and flexible products on roof top.

give a 20–25 years warranty on the products; the products also have received certification based on IECEC-61646 standards. The increasing market acceptance of a-Si:H products have led to an intense burst of activities to add new production capacity. Two large equipment manufacturers, Oerlikon (Meier *et al.*, 2008) and Applied Materials (Kadam *et al.*, 2008), are now offering large-volume production equipment to customers. Analysts expect a significant growth in production of a-Si:H PV (*PV News*, 2008) with market share increasing from about 10% today to 25% in 2012 (**Figure 45**).

We should mention that although significant reduction in module cost has taken place over the past decade, solar electricity is still not cost-competitive with base load cost of electricity generated by conventional fuels. Recognizing the importance of PV to generate clean electricity, and to reduce our dependence on fossil fuels, many countries are offering incentives to deployment of PV. This has resulted in the recent rapid growth of the PV industries. It is clearly understood by the PV community that the subsidies will not last forever, and achieving grid parity is a key challenge faced by the PV

Figure 44 World's largest roof-top PV system (12 MW) in Zaragoza, Spain, deploying a-Si:H PV products.

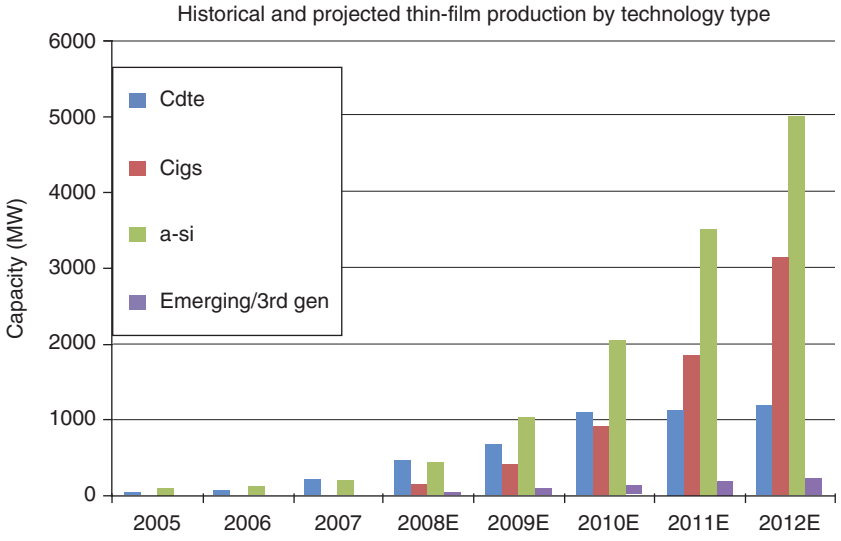

Figure 45 Growth of production capacity for different thin film technologies.

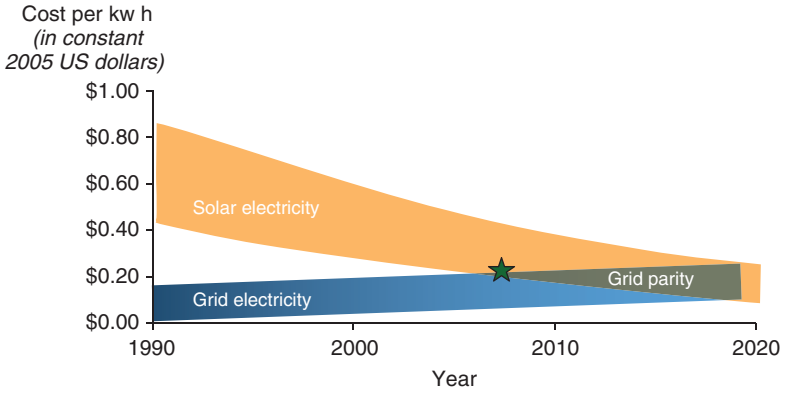

Figure 46 Path toward grid parity.

industries. **Figure 46** shows the levellized cost of electricity in 2008, and the U.S. Department of Energy Roadmap (Solar America Initiative) to reach grid parity. Extensive efforts are going on all over the world to meet this goal, and each industry has its own road map to reach grid parity.

The a-Si:H PV technology has still not reached maturity, and the potential to reduce cost is enormous. Reducing capital cost of equipment, improving machine throughput and yield, and reduction of cost of the inactive materials are some of the avenues being pursued. There is still a large gap between laboratory and production efficiency of a-Si:H modules; bridging the gap will reduce cost significantly. Even at a module efficiency of 10%, the cost can come down by a factor of 2 to be below $1 per watt (Guha, 2008, private communication). Further improvement in efficiency will reduce the cost even further.

There is an emerging need for lightweight and inexpensive solar cells for satellite, airship, and unmanned air vehicle applications. The a-Si:H has demonstrated much better stability under electron and proton bombardment than its crystalline counterparts; the defects created are annealed out under normal operating conditions in space (Guha *et al.*, 1999). This is a desirable feature for space applications, especially in the high-radiation belts. In addition to high radiation, the space environment is harsh because of temperature cycling over a wide range. Lightweight cells deposited on thin stainless steel substrates were deployed on MIR space station

for 2 years (Kagan *et al.*, 2000), and telemetry data demonstrated the reliable performance of the array. In order to increase the specific power, technology for depositing solar cells using a polyimide substrate was developed using a roll-to-roll process. An initial specific power of 1212 W kg^{-1} was demonstrated (Xu *et al.*, 2008) using a novel spray-coated encapsulation. These cells are being tested for application in airship and unmanned air vehicle. Cells deployed on an unmanned air vehicle, Zephyr, recently set a record by staying aloft for 3.5 days.

The past three decades have witnessed significant improvement in our understanding of a-Si:H alloys and devices. New materials have been invented and new processes developed. There are not too many areas of science where intellectually stimulating challenges can quickly result in a product that is of great societal benefit. Availability of clean electricity using cost-effective solar panels will have a tremendous impact on our life, and the entire a-Si:H community together with others pursuing different technologies are committed to meet this challenge.

References

Aijishi S, Smith ZE, and Wagner S (1989) Optoelectronic properties and the gap state distribution in a-SiGe alloys. In: Fritzsche H (ed.) *Amorphous Silicon and Related Materials*, pp. 887–934. Singapore: World Scientific.

Anderson J and Schulic B (2005) Performance and reliability of a 1-kW amorphous silicon photovoltaic roofing system. In: *Conference Record of the 31st IEEE Photovoltaic Specialists Conference*, pp. 1627–1630. New York: IEEE.

Arch JK, Rubinelli FA, Hou JY, and Fonash SJ (1991) Computer analysis of the role of *p*-layer quality, thickness, transport mechanisms, and contact barrier height in the performance of hydrogenated amorphous silicon *p–i–n* solar cells. *Journal of Applied Physics* 69: 7057–7066.

Banerjee A and Guha S (1991) Study of back reflectors for amorphous silicon alloy solar cell application. *Journal of Applied Physics* 69: 1030–1035.

Banerjee A, Yang J, Glatfelter T, Hoffman K, and Guha S (1994a) Experimental study of p layers in ''tunnel'' junctions for high efficiency amorphous silicon alloy multijunction solar cells and modules. *Applied Physics Letters* 64: 1517–1519.

Banerjee A, Yang J, Hoffman K, and Guha S (1994b) Characteristics of hydrogenated amorphous silicon alloy solar cells on a Lambertian back reflector. *Applied Physics Letters* 65: 472–474.

Biswas R, Li Q, Pan BC, and Yoon Y (1997) Reactive and migration of hydrogen in a-Si:H. *Materials Research Society Symposium Proceedings* 467: 135–140.

Branz HM (1998) Hydrogen collision model of light-induced metastability in hydrogenated amorphous silicon. *Solid State Communications* 105: 387–391.

Carlson DE and Wronski CR (1976) Amorphous silicon solar cell. *Applied Physics Letters* 28: 671–673.

Catalano A (1991) Solar cells made of amorphous and microcrystalline semiconductors. In: Kanicki J (ed.) *Amorphous and Microcrystalline Semiconductor Devices: Optoelectronic Devices*, p. 9. Norwood, MA: Artech House.

Catalano A and Wood G (1988) A method for improved short-wavelength response in hydrogenated amorphous silicon-based solar cells. *Journal of Applied Physics* 63: 1220–1222.

Collins RW, Ferlauto AS, Ferreira GM, *et al.* (2003) Evolution of microstructure and phase in amorphous, protocrystalline, and microcrystalline silicon studied by real time spectroscopic ellipsometry. *Solar Energy Materials and Solar Cells* 78: 143–180.

Curtins H, Wyrsch N, Favre M, and Shah AV (1987a) Influence of plasma excitation frequency for a-Si:H thin film deposition. *Plasma Chemistry and Plasma Processing* 7: 267–273.

Curtins H, Wyrsch N, and Shah A (1987b) High-rate deposition of amorphous hydrogenated silicon: Effect of plasma excitation frequency. *Electronics Letters* 23: 228–230.

Dalal VL and Baldwin G (1993) Design and fabrication of graded bandgap solar cells in amorphous Si and alloys. *Materials Research Society Symposium Proceedings* 297: 833–838.

Dalal V, Maxson T, Girvan R, and Haroon S (1997) Stability of single and tandem junction a-Si:H solar cells grown using the ECR process. *Materials Research Society Symposium Proceedings* 467: 813–817.

Das C, Cao X, Du W, Yang X, Ishikawa Y, and Deng X (2006) Effects of hydrogen dilution grading in active layer on performance of nanocrystalline single junction bottom component and corresponding a-Si:H based triple-junction solar cells. *Conference Record of the 2006 IEEE 4th World* In: *Conference on Photovoltaic Energy Conversion*, pp. 1504–1506. New York: IEEE.

Doyle JR, Doughty DA, and Gallagher A (1992a) Plasma chemistry in silane/germane and disilane/germane mixtures. *Journal of Applied Physics* 71: 4727–4738.

Doyle JR, Doughty DA, and Gallagher A (1992b) Plasma chemistry in disilane discharges. *Journal of Applied Physics* 71: 4771–4780.

Finger F, Klein S, Dylla T, Baia Neto AL, Vetterl O, and Carius R (2002) Defects in microcrystalline silicon prepared with Hot Wire CVD. *Materials Research Society Symposium Proceedings* 715: 213–224.

Fischer D, Dubail S, Anna Selvan JA, *et al.* (1996) The ''micromorph'' solar cell: Extending a-Si:H technology towards thin film crystalline silicon. In: *Proceedings of the 25th IEEE Photovoltaic Specialists Conference*, pp. 1053–1056. New York: IEEE.

Fritzsche H (1988) *Amorphous Silicon and Related Materials*. Singapore: World Scientific.

Fritzsche H (2001) Development in understanding and controlling the Staebler–Wronski effect in a-Si:H. *Annual Review of Materials Research* 31: 47–78.

Fujiwara H, Toyoshima Y, Kondo M, and Matsuda A (2000) Nucleation mechanism of microcrystalline silicon studied by real time spectroscopic ellipsometry and infrared spectroscopy. *Materials Research Society Symposium Proceedings* 609: A2.1.1–A2.1.12.

Fukawa M, Suzuki S, Guo L, Kondo M, and Matsuda A (2001) High rate growth of microcrystalline silicon using a high-pressure depletion method with VHF plasma. *Solar Energy Materials and Solar Cells* 66: 217–223.

Fukuda S, Yamamoto K, Nakajima A, *et al.* (2006) High efficiency thin film silicon hybrid cell and module with newly developed interlayer. In: Poortmans J, Ossenbrink H, Dunlop E, and Helm P (eds.) *Proceedings of the 21st European Photovoltaic Solar Energy Conference*, pp. 1535–1538. Munich, Germany: WIP Renewable Energies.

Gallagher A, Bano G, and Rozsa K (2003) Particles in silicon deposition discharges. *Solar Energy Materials and Solar Cells* 78: 27–40.

Goldstein B, Dickson CR, Campbell IH, and Fauchet PM (1988) Properties of p^+ microcrystalline films of SiC:H deposited by conventional RF glow discharge. *Applied Physics Letters* 53: 2672–2674.

Gordijn A, Francke J, Hodakova L, Rath JK, and Schropp REI (2005) Influence of pressure and plasma potential on high growth rate microcrystalline silicon growth by VHF PECVD. *Materials Research Society Symposium Proceedings* 862: 87–92.

Gordijn A, Rath JK, and Schropp REI (2006) High-efficiency μc-Si solar cells made by very high-frequency plasma-enhanced chemical vapor deposition. *Progress in Photovoltaics* 14: 305–311.

Goto M, Toyoda H, Kitagawa M, Hirao T, and Sugai H (1997) Low temperature growth of amorphous and polycrystalline silicon films from a modified inductively coupled plasma. *Japanese Journal of Applied Physics* 36: 3714–3720.

Gregg A, Parker T, and Swensen R (2005) Performance analysis of large scale, amorphous silicon, photovoltaic power systems. In: *Conference Record of the 31st IEEE Photovoltaic Specialists Conference*, pp. 1615–1618. New York: IEEE.

Guha S (2005) Can your roof provide your electrical needs? – the growth prospect of building-integrated photovoltaic. In: Conference Record of the 31st IEEE Photovoltaic Specialists Conference, pp. 12–16. New York: IEEE.

Guha S and Kulman J (1986) Fluorinated, p-Doped Microcrystalline Silicon Semiconductor Alloy Material. US Patent 4,600,801, 15 July 1986.

Guha S, Narasimhan KL, and Pietruszko SM (1981) On light-induced effect in amorphous hydrogenated silicon. *Journal of Applied Physics* 52: 859–860.

Guha S, Payson JS, Agarwal SC, and Ovshinsky SR (1987) Fluorinated amorphous silicon–germanium alloys deposited from disilane–germane mixture. *Journal of Non-Crystalline Solids* 97–98: 1455–1458.

Guha S, Xu X, Yang J, and Banerjee A (1994) High deposition rate amorphous silicon-based multijunction solar cell. *Applied Physics Letters* 66: 595–597.

Guha S and Yang J (2006) Progress in amorphous and nanocrystalline silicon. *Journal of Non-Crystalline Solids* 352: 1917–1921.

Guha S, Yang J, Banerjee A, and Sugiyama S (1998) Material issues in the commercialization of amorphous silicon alloy thin-film photovoltaic technology. *Materials Research Society Symposium Proceedings* 507: 99–105.

Guha S, Yang J, Banerjee A, Glatfelter T, and Sugiyama S (1996) Advances in amorphous silicon alloy cell and module technology. In: *International Technical Digest PVSEC-9*, p. 283. Tokyo, Japan.

Guha S, Yang J, Banerjee A, Hoffman K, and Call J (1999a) Manufacturing issues for large volume production of amorphous silicon photovoltaic modules. *AIP Conference Proceedings* 462: 88–93.

Guha S, Yang J, Jones SJ, Chen Y, and Williamson DL (1992) Effect of microvoids on initial and light-degraded efficiencies of hydrogenated amorphous silicon alloy solar cells. *Applied Physics Letters* 61: 1444–1446.

Guha S, Yang J, Nath P, and Hack M (1986) Enhancement of open circuit voltage in high efficiency amorphous silicon alloy solar cells. *Applied Physics Letters* 49: 218–220.

Guha S, Yang J, Pawlikiewicz A, Glatfelter T, Ross R, and Ovshinsky SR (1989) Band-gap profiling for improving the efficiency of amorphous silicon alloy solar cells. *Applied Physics Letters* 54: 2330–2332.

Guha S and Yang CC (1992) Method for Manufacture of Improved Efficiency Tandem Photovoltaic and Device Manufacture Thereby. US Patent 5298086, 29 March 1994.

Guha S, Yang J, Williamson DL, Lubianiker Y, Cohen JD, and Mahan AH (1999b) Structural, defect, and device behavior of hydrogenated amorphous Si near and above the onset of microcrystallinity. *Applied Physics Letters* 74: 1860–1862.

Guha S, Yang J, Banerjee A, *et al.* (1999c) Low cost and lightweight amorphous silicon alloy solar array for space application. In: *Proceedings of the 14th Intersociety Energy Conversion Engineering Conference*, p.1, Vancouver, Canada.

Guo L, Kondo M, Fukawa M, Saitoh K, and Matsuda A (1998) High rate deposition of microcrystalline silicon using conventional plasma-enhanced chemical vapor deposition. *Japanese Journal of Applied Physics* 37: L1116–L1118.

Haase C and Stiebig H (2006) Optical properties of thin-film silicon solar cells with grating couplers. *Progress in Photovoltaics: Research and Applications* 14: 629–641.

Hack M and Shur M (1985) Physics of amorphous silicon p–i–n solar cells. *Journal of Applied Physics* 59: 998–1020.

Hamers EAG, Lenssen JMT, Borreman A, *et al.* (2008) Manufacturing of large area thin film silicon flexible solar cell modules employing a temporary superstrate foil. In: *Proceedings of the 23rd European Photovoltaic Solar Energy Conference*, pp. 2065–2068. Munich, Germany: WIP Renewable Energies.

Hanaki K, Hattori Y, Nakabayashi H, Yamaguchi S, and Hamakawa Y (1989) A semi-transparent solar cell using a-SiC. *Materials Research Society Symposium Proceedings* 149: 395–404.

Hattori Y, Kruangam YD, Katoh K, Nitta Y, Okamoto H, and Hamakawa Y (1987) High-conductivity wide band gap p-type a-SiC:H prepared by ECR CVD and its application to high efficiency a-Si based solar cells. In: *Conference Record of the 19th IEEE Photovoltaic Specialists Conference*, pp. 689–694. New York: IEEE.

Hegedus S, Sopori B, and Paulson PD (2002) Optical design and analysis of textured a-Si:H solar cells. In: *Conference Record of the 29th IEEE Photovoltaic Specialists Conference*, pp. 1122–1125. New York: IEEE.

Hoffman K and Glatfelter T (1993) An optical study of each layer in a-Si:H solar cells. In: *Conference Record of the 23rd IEEE Photovoltaic Specialists Conference*, pp. 986–990. New York: IEEE.

Hou JH, Arch JK, Fonash SJ, Wiedeman S, and Bennett M (1991) An examination of the ''tunnel junctions'' in triple junction a-Si:H based solar cells: Modeling and effects on performance. In: *Conference Record of the 22nd IEEE Photovoltaic Specialists Conference*, pp. 1260–1264. New York: IEEE.

Hugger PG, Cohen D, Yue G, Yan B, Yang J, and Guha S (2008) Properties of light-induced degradation and the electronic properties of nanocrystalline silicon solar cells grown under functionally graded hydrogen dilutions. *Journal of Non-Crystalline Solids* 354: 2460–2463.

Ichikawa Y, Aizawa K, Shimabukuro H, Nagao Y, and Sakai H (1987) Deposition process and film properties of a-Si alloy films. In: *Technical Digest of 3rd International Photovoltaic Science and Engineering Conference*, p. 29. Tokyo, Japan.

Izu M and Ellison T (2003) Roll-to-roll manufacturing of amorphous silicon alloy solar cells *in situ* cell performance diagnostics. *Solar Energy Materials and Solar Cells* 78: 613–626.

Jiang C-S, Yan B, Yan Y, *et al.* (2008) P-induced nanocrystalline dispersion in amorphous-nanocrystalline mixed-phase Si:H thin films. *Journal of Applied Physics* 103: 063515.

Kadam A, Li L, Sheng S, *et al.* (2008) Development of highly efficient a-Si:H/μc-Si:H tandem thin film solar cells on 5.7 m^2 size glass substrates. In: *Proceedings of the 23rd*

European Photovoltaic Solar Energy Conference, pp. 2062–2064. Munich, Germany: WIP Renewable Energies.

Kagan M, Nadorov V, Guha S, Yang J, and Banerjee A (2000) Space qualification of amorphous silicon alloy lightweight modules. In: *Conference Record of the 28th IEEE Photovoltaic Specialists Conference*, pp. 1261–1264. New York: IEEE.

Kamei T, Hata N, Matsuda A, *et al.* (1996) Deposition and extensive light soaking of highly pure hydrogenated amorphous silicon. *Applied Physics Letters* 68: 2380–2382.

Kamei T, Stradins P, and Matsuda A (1999) Effects of embedded crystallites in amorphous silicon on light-induced defect creation. *Applied Physics Letters* 74: 1707–1709.

Kinoshita T, Isomura M, Hishikawa Y, and Tsuda Y (1996) Influence of oxygen and nitrogen in the intrinsic layer of a-Si:H solar cells. *Japanese Journal of Applied Physics* 35: 3819–3824.

Klein S, Finger F, Carius R, *et al.* (2003) Intrinsic microcrystalline silicon prepared by hot-wire chemical vapor deposition for thin film solar cells. *Thin Solid Films* 430: 202–207.

Koh J, Ferlauto AS, Rovira PI, Wronski CR, and Collins RW (1999) Evolutionary phase diagrams for plasma-enhanced chemical vapor deposition of silicon thin films from hydrogen-diluted silane. *Applied Physics Letters* 75: 2286–2288.

Koh J, Lee Y, Fujiwara H, Wronski CR, and Collins RW (1998) Optimization of hydrogenated amorphous silicon *p–i–n* solar cells with two-step *i* layers guided by real-time spectroscopic ellipsometry. *Applied Physics Letters* 73: 1526–1578.

Kondo M (2003) Microcrystalline materials and cells deposited by RF glow discharge. *Solar Energy Materials and Solar Cells* 78: 543–566.

Kondo M, Matsui T, Nasuno Y, *et al.* (2005) Crucial processing steps for microcrystalline silicon bottom cells. In: *Proceedings of 31st IEEE Photovoltaic Specialists Conference*, pp. 1377–1382. New York: IEEE.

Krc J, Zeman M, Campa A, Smole F, and Topic M (2006) Novel approaches of light management in thin-film silicon solar cells. *Materials Research Society Symposium Proceedings* 910: 669–680.

Kroll U, Meier J, Keppner H, *et al.* (1995) Origin and incorporation mechanism for oxygen contaminations in a-Si:H and μc-Si:H films prepared by the very high frequency (70 MHz) glow discharge technique. *Materials Research Society Symposium Proceedings* 377: 39–44.

Lechner P, Frammelberger W, Psyk W, *et al.* (2008) Status of performance of thin film silicon solar cells and modules. In: *Proceedings of the 23rd European Photovoltaic Solar Energy Conference*, pp. 2023–2026. Munich, Germany: WIP Renewable Energies.

Li YM (1993) Amorphous silicon–carbon alloys for solar cells. *Materials Research Society Symposium Proceedings* 297: 803–814.

Longeaud C, Kleider PJ, Roca i Cabarrocas P, Hamma S, Meaudre R, and Meaudre M (1998) Properties of a new a-Si:H like materials: Hydrogenated polymorphous silicon. *Journal of Non-Crystalline Solids* 227–230: 96–99.

Luft W and Tsuo YS (1993) *Hydrogenated Amorphous Silicon Alloy Deposition Process*. New York: Marcel Dekker.

Mahan AH (2003) Hot wire chemical vapor deposition of Si containing materials for solar cells. *Solar Energy Materials and Solar Cells* 78: 299–328.

Mahan AH, Calapella J, Nelson BP, Crandall RS, and Balberg I (1991) Deposition of device quality, low H content amorphous silicon. *Journal of Applied Physics* 69: 6728–6730.

Mahan AH, Reedy RC, Jr., Iwaniczko E, *et al.* (1998) H out-diffusion and device performance in n–i–p solar cells utilizing high temperature hot wire a-Si:H i-layers. *Materials Research Society Symposium Proceedings* 507: 119–130.

Mashima H, Yamakoshi H, Kawamura K, *et al.* (2006) Large area VHF plasma production using a ladder-shaped electrode. *Thin Solid Films* 506–507: 512–516.

Matsuda A (1999) Growth mechanism of microcrystalline silicon obtained from reactive plasmas. *Thin Solid Films* 337: 1–6.

Matsuda A, Kaga T, Tanaka H, and Tanaka K (1983) Lifetime of dominant radicals for the deposition of a-Si:H from SiH4 and Si2H6 glow discharges. *Journal of Non-Crystalline Solids* 59/60: 687–690.

Matsuda A, Takai M, Nishimoto T, and Kondo M (2003) Control of plasma chemistry for preparing highly stabilized amorphous silicon at high growth rate. *Solar Energy Materials and Solar Cells* 78: 3–26.

Matsuda A and Tanaka K (1982) Plasma spectroscopy-glow discharge deposition of hydrogenated amorphous silicon. *Thin Solid Films* 92: 171–187.

Matsumura H (1987) Study on catalytic chemical vapor deposition methods to prepare hydrogenated amorphous silicon. *Journal of Applied Physics* 65: 4396–4398.

Matsumura H and Tachibana H (1985) Amorphous silicon produced by a new thermal chemical vapor deposition method using intermediate species SiF2. *Applied Physics Letters* 47: 833–835.

Meaudre M, Meaudre R, Butté R, *et al.* (1999) Midgap density of states in hydrogenated polymorphous silicon. *Journal of Applied Physics* 86: 946–950.

Meier J, Flückiger R, Keppner H, and Shah A (1994) Complete microcrystalline *p–i–n* solar cell-crystalline or amorphous cell behavior? *Applied Physics Letters* 65: 860–862.

Meier J, Kroll U, Benagli S, *et al.* (2008) Latest R&D developments of thin film silicon PV at Oerlikon Solar. In: *Proceedings of the 23rd European Photovoltaic Solar Energy Conference*, pp. 2057–2061. Munich, Germany: WIP Renewable Energies.

Meier J, Torres P, Platz R, *et al.* (1996) On the way towards high efficiency thin film silicon solar cells by ''micromorph'' concept. *Materials Research Society Symposium Proceedings* 420: 3–14.

Meillaud F, Shah S, Droz C, Vallat-Sauvain E, and Miazza C (2006) Efficiency limits for single-junction and tandem solar cells. *Solar Energy Materials and Solar Cells* 90: 2952–2959.

Michelson CE, Gelatos AV, and Cohen JD (1985) Drive-level capacitance profiling: Its application to determining gap state densities in hydrogenated amorphous silicon films. *Applied Physics Letters* 47: 412–414.

Miller D, Lutz H, Weismann H, *et al.* (1978) Some properties of evaporated amorphous silicon made with atomic hydrogen. *Journal of Applied Physics* 49: 6192–6193.

Möbius I, van Cleef M, Chianese D, and Pola I (2008) Comparison of yield, installed power and costs of a typical installation for flat roofs for triple-junction and crystalline modules. In: *Proceedings of the 23rd European Photovoltaic Solar Energy Conference*, pp. 3092–3095. Munich, Germany: WIP Renewable Energies.

Moustakas T, Maruska H, and Friedman R (1985) Properties and photovoltaic applications of microcrystalline silicon films prepared by RF reactive sputtering. *Journal of Applied Physics* 58: 983–986.

Nakata Y, Sannomiya H, Moriuchi S, *et al.* (1990) Study of bandgap profiling control on photovoltaic performance in three stacked amorphous solar cells. *Materials Research Society Symposium Proceedings* 192: 15.

Nakatani K, Yano M, Suzuki K, and Okaniwa H (1983) Properties of microcrystalline P doped Si:H films. *Journal of Non-Crystalline Solids* 59–60: 827–830.

Nasuno Y, Kondo M, and Matsuda A (2000) Microcrystalline silicon thin-film solar cells prepared at low temperature using RF-PECVD. In: *Proceedings of the 28th IEEE*

Photovoltaic Specialists Conference, pp. 142–145. New York: IEEE.

Nikolaeva-Dimitrova M, Skoczek A, Kenny RP, and Dunlop ED (2008) Outdoor module performance of single, double and triple-junction silicon based thin film technologies. In: Proceedings of the 23rd European Photovoltaic Solar Energy Conference, pp. 2079–2083. Munich, Germany: WIP Renewable Energies.

Nomoto K, Takeda Y, Moriuchi S, *et al.* (1989) Properties of hydrogen diluted a-SiC:H film and its application to amorphous solar cells. In: *International Technical Digest of the 4th International Photovoltaic Science and Engineering Conference*, p. 85. Tokyo, Japan.

Nuruddin A, Doyle JR, and Abelson JR (1992) Macro-trench studies of surface reaction probability of a-Si:H film growth. *Materials Research Society Symposium Proceedings* 258: 33–37.

Pawlikiewicz AH and Guha S (1990) Numerical modeling of an amorphous-silicon-based p–i–n solar cell. *IEEE Transactions on Electron Devices* 37: 403–409.

Pethe SA, Kaul A, and Dhere NG (2008) Statistical data analysis of thin film photovoltaic modules deployed in hot and humid climate of Florida. *Proceedings of the SPIE* 7048: 70480T-1–70480T-8.

Pillai S, Catchpole KR, Trupke T, and Green MA (2007) Surface plasmon enhanced silicon solar cells. *Journal of Applied Physics* 101: 093105.

Poruba A, Fejfar A, Reme Z, *et al.* (2000). Optical absorption and light scattering in microcrystalline silicon thin films and solar cell. *Journal of Applied Physics* 88: 148–160.

PV News August 2008.

Robertson J (2000a) Deposition mechanism of hydrogenated amorphous silicon. *Journal of Applied Physics* 87: 2608–2617.

Robertson J (2000b) Growth process of hydrogenated amorphous silicon. *Materials Research Society Symposium Proceedings* 609: A1.4.1–A1.4.12.

Roca i Cabarrocas P (2000) Plasma enhanced chemical vapor deposition of amorphous, polymorphous and microcrystalline silicon films. *Journal of Non-Crystalline Solids* 266: 31–37.

Roschek T, Repmann T, Müller J, Rech B, and Wagner H (2000) High rate deposition of microcrystalline silicon solar cells using 13.56 MHz PECVD. In: *Proceedings of the 28th IEEE Photovoltaic Specialists Conference*, pp. 150–153. New York: IEEE.

Rubinelli FA, Jiménez R, Rath JK, and Schropp REI (2002) Using computer modeling analysis in single junction a-SiGe:H *p–i–n* solar cells. *Journal of Applied Physics* 91: 2409–2416.

Sakamoto Y (1977) Measurement of power transfer efficiency from microwave field to plasma under ECR condition. *Japanese Journal of Applied Physics* 16: 1993–1998.

Schropp RIE and Zeman M (1998) *Amorphous and Microcrystalline Solar Cells: Modeling, Materials, and Device Technology*. Dordrecht: Kluwer.

Shah A, Dutta J, Wyrsch N, *et al.* (1992) VHF plasma deposition: A comparative overview. *Materials Research Society Symposium Proceedings* 258: 15–26.

Shah AV, Meier J, Vallat-Sauvain E, *et al.* (2003) Material and solar cell research in microcrystalline silicon. *Solar Energy Materials and Solar Cells* 78: 469–491.

Shibata N, Fukuda K, Ohtoshi H, Hanna J, Oda S, and Shimizu I (1987) Growth of amorphous and crystalline silicon by – HR-CVD hydrogen radical enhanced CVD. *Materials Research Society Symposium Proceedings* 95: 225–235.

Shimizu T, Kumeda M, Morimoto A, Tsujimura Y, and Kobayashi I (1986) NMR and ESR studies on a-$Si_{1-x}Ge_x$:H films prepared by glow discharge and magnetron sputtering. *Materials Research Society Symposium Proceedings* 70: 313–318.

Sopori B, Madjdpour J, Zhang Y, *et al.* (1999) Optical modeling of a-Si solar cells. *Materials Research Society Symposium Proceedings* 557: 755–760.

Spear WE and LeComber PG (1975) Substitutional doping of amorphous silicon. *Solid State Communications* 17: 1193–1196.

Sriraman S, Agarwal S, Aydil ES, and Maroudas D (2002) Mechanism of hydrogen-induced crystallization of amorphous silicon. *Nature* 418: 62–65.

Staebler DL and Wronski CR (1977) Reversible conductivity changes in discharge-produced amorphous Si. *Applied Physics Letters* 31: 292–294.

Street RA (1991) *Hydrogenated Amorphous Silicon*. Cambridge: Cambridge University Press.

Stutzmann M, Jackson WB, and Tsai CC (1985) Light-induced metastable defects in hydrogenated amorphous silicon: A systematic study. *Physical Review B* 32: 23–47.

Takagi T, Ueda M, Ito N, Watabe Y, Sato H, and Sawaya K (2006) Large area VHF plasma sources. *Thin Film Solids* 502: 50–54.

Takano A, Tabuchi K, Uno M, *et al.* (2006) Production technologies of film solar cell. *Materials Research Society Symposium Proceedings* 910: 687–695.

Takatsuka H, Yamauchi Y, Fukagawa M, *et al.* (2006a) High efficiency thin film solar modules. In: *21st European Photovoltaic Solar Energy Conference*, pp. 1531–1534. Munich, Germany: WIP Renewable Energies.

Takatsuka H, Yamauchi Y, and Takeushi Y (2006b) The world's largest high efficiency thin film silicon solar cell module. In: *Conference Record of the 2006 IEEE 4th World Conference on Photovoltaic Energy Conference*, pp. 2028–2033. New York: IEEE.

Tawada Y, Hamagishi H, and Yamamoto K (2004) Mass production of large-area integrated thin-film silicon solar-cell module. In: Hamakawa Y (ed.) *Thin-Film Solar Cells*, pp. 150–161. Berlin: Springer.

Tawada Y, Tsuge K, Kondo M, Okamoto H, and Hamakawa Y (1982) Properties and structure of a-SiC:H for high-efficiency a-Si solar cell. *Journal of Applied Physics* 53: 5273–5281.

Teplin CW, Jiang C-S, Stradins P, and Branz HM (2008) Cone kinetics model for two-phase film silicon deposition. *Applied Physics Letters* 92: 093114.

Tsai CC, Anderson GB, Thompson R, and Wacker B (1989) Control of silicon network structure in plasma deposition. *Journal of Non-Crystalline Solids* 114: 151–153.

Tsai CC, Stutzmann M, and Jackson WB (1984) The Staebler-Wronski effect in undoped a-Si:H its intrinsic nature and the influence of impurities. In: *AIP Conference Proceedings* 120: 242–249.

Tsu R, Chao SS, Izu M, Ovshinsky SR, Jan GJ, and Pollack FH (1981) The nature of intermediate range order in Si:F:H:(p) alloy systems. *Journal of Physics* C4: 269–272.

Tsu DV, Chao BS, Ovshinsky SR, Guha S, and Yang J (1997) Effect of hydrogen dilution on the structure of amorphous silicon alloys. *Applied Physics Letters* 71: 1317–1319.

van Cleef M, Lippens P, and Call J (2001) Superior energy yields of Uni-Solar® triple junction thin film silicon solar cells compared to crystalline silicon solar cells under real outdoor conditions in western Europe. In: *Proceedings of the 17th European Photovoltaic Solar Energy Conference.* Munich, Germany, 22–26 October.

van de Sanden MCM, Severens RJ, Kessels WMM, Meulenbroeks RFG, and Schram DC (1998) Plasma chemistry aspects of a-Si:H deposition using an expanding thermal plasma. *Journal of Applied Physics* 84: 2426–2435.

Wang Q, Antoniadis H, Schiff EA, and Guha S (1993) Electron-drift-mobility measurements and exponential conduction-band tails in hydrogenated amorphous silicon–germanium alloys. *Physical Review B* 47: 9435–9448.

Wang Q, Crandall RS, and Schiff EA (1996) Field collapse due to band-tail charge in amorphous silicon solar cells. In: *Conference Record of the 25th IEEE Photovoltaic Specialists Conference*, pp. 1113–1116. New York: IEEE.

Wang C and Lucovsky G (1990) Intrinsic microcrystalline silicon deposited by remote PECVD: A new thin film photovoltaic material. In: *Proceedings of the 21st IEEE Photovoltaic Specialists Conference*, pp. 1614–1618. New York: IEEE.

Williams MJ, Cho SM, and Lucovsky G (1993) Hydrogenated amorphous silicon–nitrogen, a-Si,N:H alloys: An alternative to a-Si,C:H for the wide band gap photo-active material in tandem PV cells. *Materials Research Society Symposium Proceedings* 297: 759–764.

Williamson DL (1995) Nanostructure of a-Si:H and related materials by small-angle X-ray scattering. *Materials Research Society Symposium Proceedings* 377: 251.

Williamson D (2003) Microstructure of amorphous and microcrystalline Si and SiGe alloys using X-rays and neutrons. *Solar Energy Materials and Solar Cells* 78: 41–84.

Xu X, Lord K, Pietka G, *et al.* (2008) *Conference Record of the 33rd IEEE Photovoltaic Specialists Conference*, Paper No. 246 (CD). New York: IEEE.

Xu X, Yang J, and Guha S (1993) On the lack of correlation between film properties and solar cell performance of amorphous silicon–germanium alloys. *Applied Physics Letters* 62: 1399–1401.

Xu X, Yang J, and Guha S (1996) Hydrogen dilution effects on a-Si:H and a-SiGe:H materials properties and solar cell performance. *Journal of Non-Crystalline Solids* 198–200: 60–64.

Yablonovitch E (1982) Statistical ray optics. *Journal of the Optical Society of America* 72: 899–907.

Yablonovitch E and Cody GD (1982) Intensity enhancement in textured optical sheets for solar cells. *IEEE Transactions on Electron Devices* ED-29: 303–305.

Yamamoto K (1999) Very thin film crystalline silicon solar cells on glass substrate fabricated at low temperature. *IEEE Transactions on Electron Devices* 46: 2041–2047.

Yamamoto K, Nakajima A, Yoshimi M, *et al.* (2003) Novel hybird thin film silicon solar cell and module. In: *Proceedings of the 3rd World Conference on Photovoltaic Energy Conversion*, p. 2789. Osaka, Japan: Photovoltaic Science and Engineering Conference Committee.

Yan B, Lord K, Yang J, Guha S, Smeets J, and Jacquet J-M (2002) Hydrogenated microcrystalline silicon solar cells made with modified very-high-frequency glow discharge. *Materials Research Society Symposium Proceedings* 715: 629–634.

Yan B, Owens JM, Jiang C-S, Yang J, and Guha S (2005) Improved back reflector for high efficiency hydrogenated amorphous and nanocrystalline silicon based solar cells. *Materials Research Society Symposium Proceedings* 862: 603–608.

Yan B, Yang J, Guha S, and Gallagher A (1999) Analysis of plasma properties and deposition of amorphous silicon alloy solar cells using very high frequency glow discharge. *Materials Research Society Symposium Proceedings* 557: 115–120.

Yan B, Yang J, Lord K, and Guha S (2001) Annealing kinetics of amorphous silicon alloy solar cells made at various deposition rates. *Materials Research Society Symposium Proceedings* 664: A25.2.1–A25.2.6.

Yan B, Yue G, Banerjee A, Yang J, and Guha S (2004a) Large-area hydrogenated amorphous and microcrystalline silicon double-junction solar cells. *Materials Research Society Symposium Proceedings* 808: 581–586.

Yan B, Yue G, Jiang C-S, *et al.* (2008a) Optical enhancement by textured back reflector in amorphous and nanocrystalline silicon based solar cells. *Materials Research Society Symposium Proceedings* E1101.

Yan B, Yue G, Owens JM, Yang J, and Guha S (2004b) Light-induced metastability in hydrogenated nanocrystalline silicon solar cells. *Applied Physics Letters* 85: 1925–1927.

Yan B, Yue G, Owens JM, Yang J, and Guha S (2006) Over 15% efficient hydrogenated amorphous silicon based triple-junction solar cells incorporating nanocrystalline silicon. *Conference Record of the 2006 IEEE 4th World Conference on Photovoltaic Energy Conversion*, pp. 1477–1480. New York: IEEE.

Yan B, Yue G, Yan Y, *et al.* (2008b) Correlation of hydrogen dilution profiling to material structure and device performance of hydrogenated nanocrystalline silicon solar cells. *Materials Research Society Symposium Proceedings* 1066: 61–66.

Yan B, Yue G, Yang J, Banerjee A, and Guha S (2003a) Hydrogenated microcrystalline silicon single-junction and multi-junction solar cells. *Materials Research Society Symposium Proceedings* 762: 309–318.

Yan B, Yue G, Yang J, Lord K, Banerjee A, and Guha S (2003b) Microcrystalline silicon solar cells made using RF, MVHF, and microwave at various deposition rates. In: *Proceedings of the 3rd World Conference on Photovoltaic Energy Conversion*, p. 2773. Osaka, Japan: Photovoltaic Science and Engineering Conference Committee.

Yan B, Yue G, Yang J, and Guha S (2008c) Correlation of current mismatch and fill factor in amorphous and nanocrystalline silicon based high efficiency multi-junction solar cells. In: *Proceedings of the 33rd IEEE Photovoltaic Specialists Conference,* Paper No. 257 (CD). New York: IEEE.

Yan B, Yue G, Yang J, *et al.* (2004c) Hydrogen dilution profiling for hydrogenated microcrystalline silicon solar cells. *Applied Physics Letters* 85: 1955–1957.

Yan B, Yue G, Yang J, *et al.* (2004d) Microstructure evolution with thickness and hydrogen dilution profile in microcrystalline silicon solar cells. *Materials Research Society Symposium Proceedings* 808: 575–580.

Yang J, Banerjee A, Glatfelter T, Hoffman K, Xu X, and Guha S (1994) Progress in triple-junction amorphous silicon-based alloy solar cells and modules using hydrogen dilution. In: *First World Conference on Photovoltaic Energy Conversion Proceedings*, 380. New York: IEEE.

Yang J, Banerjee A, and Guha S (1997) Triple-junction amorphous silicon alloy solar cell with 14.6% initial and 13% stable conversion efficiencies. *Applied Physics Letters* 70: 2975–2977.

Yang J, Banerjee A, and Guha S (2003) Amorphous silicon based photovoltaics – from earth to the ''final frontier. *Solar Energy Materials and Solar Cells* 78: 597–612.

Yang J, Xu X, Banerjee A, and Guha S (1996) Progress in triple-junction amorphous silicon alloy solar cells with improved current mismatch in component cells. In: *Conference Record of the 25th IEEE Photovoltaic Specialists Conference*, pp. 1041–1046. New York: IEEE.

Yoshida T, Tabuchi K, Takano A, *et al.* (2000) Fabrication of a-Si/a-SiGe/a-SiGe triple-junction plastic film substrate solar cells. In: *Conference Record of the 28th IEEE Photovoltaic Specialists Conference*, p. 762. New York: IEEE.

Yue G, Yan B, Ganguly G, *et al.* (2006) Performance improvement of hydrogenated nanocrystalline silicon solar cells by hydrogen dilution profiling. In: *Conference Record of the 2006 IEEE 4th World Conference on Photovoltaic Energy Conference*, pp. 1588–1591. New York: IEEE.

Yue G, Yan B, Teplin C, Yang J, and Guha S (2008) Optimization and characterization of *i/p* buffer layer in hydrogenated nanocrystalline silicon solar cells. *Journal of Non-Crystalline Solids* 354: 2440–2443.

Yue G, Yan B, Yang J, and Guha S (2005a) Effect of electrical bias on metastability in hydrogenated nanocrystalline silicon solar cells. *Applied Physics Letters* 86: 092103.

Yue G, Yan B, Yang J, and Guha S (2005b) Enhancement of light-induced degradation under reverse bias in

hydrogenated nanocrystalline silicon solar cells. *Journal of Applied Physics* 98: 074902.
Yue G, Yan B, Yang J, and Guha S (2007) High rate deposition of amorphous silicon based solar cells using modified very high frequency glow discharge. *Materials Research Society Symposium Proceedings* 989: 359–364.
Zhou D and Biswas R (2008) Photonic crystal enhanced light-trapping in thin film solar cells. *Journal of Applied Physics* 103: 093102.
Zimmer J, Stiebig H, Folsch J, Finger F, Eickhoff T, and Wagner H (1997) More insights into band gap graded a-SiGe:H solar cells by experimental and simulation data. *Materials Research Society Symposium Proceedings* 467: 735–740.
Zimmer J, Stiebig H, and Wagner H (1998) a-SiGe:H based solar cells with graded absorption layer. *Journal of Applied Physics* 84: 611–617.

Further Reading

Arya R, Oswald R, Li Y, *et al.* (1994) Progress in amorphous silicon based multijunction modules. In: *Proceedings of the 1st World Conference on Photovoltaic Energy Conversion*, pp. 394–400. New York: IEEE.
Banerjee A, Yang J, and Guha S (1999). Optimization of high efficiency amorphous silicon alloy based triple-junction modules. *Materials Research Society Symposia Proceedings* 557: 743–748.
Guha S and Fritzsche H (eds.) (2003) *Special Issue: Solar Energy Materials and Solar Cells* 78: 1–688.
Luque A and Hegedus S (eds.) (2003) *Handbook of Photovoltaic Science and Engineering*. Chichester: Wiley.
Mai Y, Klein S, Carius R, Stiebig H, Geng X, and Finger F (2005) Open circuit voltage improvement of high-deposition-rate microcrystalline silicon solar cells by hot wire interface layers. *Applied Physics Letters* 87: 073503.
Okamoto S, Terakawa A, Maruyama E, Shinohara W, Tanaka M, and Kiyama S (2001). Towards stabilized 10% efficiency of large-area (> 5000 cm^2) a-Si/a-SiGe tandem solar cells using high-rate deposition. *Materials Research Society Symposium Proceedings* 664: A11.1.1–A11.11.10.
Rech B, Muller J, Repmann T, *et al.* (2003) Amorphous and microcrystalline silicon solar cells and module on textured zinc oxide coated glass substrates. *Materials Research Society Symposium Proceedings* 762: 285–295.
Sakai H, Yoshida T, Fujikake S, and Ichikawa Y (1989) Double-stacked a-Si/a-Si and a-SiC/a-Si tandem solar cells with high efficiency and high reliability. *Materials Research Society Symposium Proceedings* 149: 477–482.
Saito K, Sano M, Okabe S, Sugiyama S, and Ogawa K (2005) Microcrystalline silicon solar cells fabricated by VHF plasma CVD method. *Solar Energy Materials and Solar Cells* 86: 565–575.
Schropp EIR and Zeman M (1998) *Amorphous and Microcrystalline Silicon Solar Cells*. Boston, MA: Kluwer.
Yamamoto K, Nakajima A, Yoshimi M, *et al.* (2002) High efficiency thin film silicon solar cell and module. In: *Proceedings of the 29th IEEE Photovoltaic Specialists Conference,* pp. 1110–113. New York: IEEE.

Relevant Websites

http://www.flexcell.com – Flexible photovoltaic cell manufacturer.
http://www.kaneka.com – Kaneka Thin-film Silicon Report.
http://www.nrel.gov – National Renewable Energy Laboratory.
http://www.powerfilmsolar.com – PowerFilm is a developer and manufacturer of thin, flexible solar panels based on a proprietary low-cost production process.
http://www.uni-solar.com – UNI-SOLAR is the world leader in flexible solar modules.